# From millions of years to milliseconds in subduction earthquake sequence models

Master thesis Earth, Structure and Dynamics

**Name:** Mhina de Vos

**Studentnumber:** 5868521

**Email:** m.s.devos@students.uu.nl

**Date:** 30 March 2023

**Supervisors:** Dr. Ylona v. Dinther (UU) and Prof. Dr. Taras Gerya (ETH)

# 1 Abstract

I succeeded to cross the time scale from millions of years to milliseconds for the first time. This large numerical accomplishment is of enormous importance to completely understand the physics of a subduction zone setting. The models solves the governing equations for a visco-elasto-plastic rheology on a staggered grid with Lagrangian markers. During the subduction zone evolution the Drucker-Prager yield condition is applied and it switches to the invariant formulation of the rate- and state-dependent friction with adaptive time stepping in the seismic cycle. The long term model takes up to 4 million years in which the oceanic plate slowly subducts into the mantle, when switching to the short-term seismic cycle the megathrust locks and builds up stress at the plate interface. The oceanic crust consist out of a 5 kilometer thick gabbro layer overlain by 2 kilometer of faultrock. I have increased the pore fluid rate, $\lambda = 0.95$, and implemented temperature dependent weakening and cohesion on the fault rock. All other rocktypes are velocity strengthening with a cohesion of 200 MPa, to make sure that faulting is localised on the fault rock. In my reference simulation two slow slip events occur before an earthquake develops. The main earthquake nucleates at a depth of 30 kilometer, takes 100 seconds and is 24 minutes earlier preceded by a fore-shock at a depth of 60 kilometers. The maximum slip rate is 6.3 m/s and is resolved with a minimum time step of $4.0 * 10^{-3}$ seconds. The slip on the megathrust is continuously and has a crack-like behaviour with most of the slip occurring at the downdip and updip limit of the seismogenic zone. Velocity strengthening sediments that were brought down during the long term part causes a heterogeneous distribution of slip and stress change. With the model it is also possible to generate slow slip events, which can be classified into two classes. The first class has a maximum velocity in the order of $10^{-8}$ m/s, slip only occurs on the lower part of the megathrust and it takes years to complete. The second class has a maximum velocity in the order of $10^{-4}$ m/s with slip reaching almost the surface and it takes multiple days to a month to complete. Whether the simulation produces (a)seismic events is dependent on the direct effect (a), the evolutionary effect (b) and the characteristic slip distance (L). There are four regimes present in our model and these are comparable to other studies: 1. Stable sliding with decaying oscillations. 2. Periodic slow slip events 3. Multiple slow slip events followed by one earthquake and after that stable sliding 4. Multiple slow slip events and earthquakes.

# 2 Introduction

Subduction zones settings are the most dangerous plate boundaries on earth, where great megathrust earthquakes with catastrophic consequences can occur [Wirth et al., 2022]. Three examples of the last two decades are the Tohoku-oki earthquake in Japan in 2011 with a magnitude of 9.0 [Kajitani et al., 2013; Sato et al., 2011], the Maule earthquake in Chili in 2010 with a magnitude of 8.8 [Vigny et al., 2011] and the Sumatra-Andaman earthquake in Indonesia in 2004 with a magnitude of 9.2 [Lay et al., 2005].
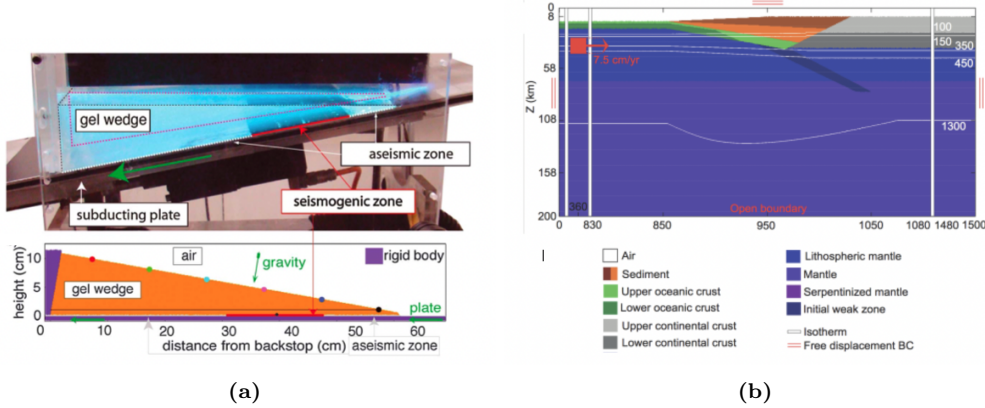
**Figure 1:** A) Analog (top) and numerical (bottom) setup of Van Dinther et al. [2013b]. Both gelatin wedges have a visco-elastic rheology, while the gelatin-sand paper (red) and gelatin-plastic (grey) interactions are represented by a visco-elasto-plastic fault zone. B) Initial setup of numerical model representing Southern Chili of Van Dinther et al. [2013a]. Colors represent the different rocktypes, which are overlain by the isotherms in white.

Seismicity at a subduction plate interface accounts for approximately 90% of the total seismic moment that has been released in the in the last century [Heuret et al., 2011]. The contribution of the seismic moment is uneven distributed over the globe with large events being restricted to a subset of convergent margins [Heuret et al., 2011]. A lot of research has been done to describe the variability of subduction plate interfaces and link it to tectonic parameters [e.g. Uyeda and Kanamori [1979]; Ruff and Kanamori [1980]; Jarrard [1986]]. Numerous parameters have been suggested such as the convergence rate, plate age and lithological heterogeneity [Wirth et al., 2022]. Heuret et al. [2011] performed a statistical analysis to identify the features that causes earthquakes in subduction plate interfaces. By correlating between significant parameters they find out that the seismic rate increases with larger and steeper plate interfaces which occur in fast subduction zones with cold slabs. And that events with $Mw > 8.5$ take place near slab edges, where the upper plate is continental and the back-arc strain neutral [Heuret et al., 2011].

To completely understand the physical mechanisms of megathrust earthquakes geophysical-, paleoseismic-, geological observations and physical properties have to be combined with numerical models [Wirth et al., 2022]. Using numerical models eliminates the spatial-temporal limitations of direct observations, but making these models is challenging both scientifically and methodologically [Gerya, 2022]. There are several numerical models simulating a subduction zone, but in most models the long term deformation is simulated separately from the earthquakes and the seismic cycle [Gerya, 2022]. The classical simulations of earthquake cycles use a pre-defined, discrete fault embedded in a elastic medium. While long term evolution models use evolving faults without accounting for inertial forces and with large time steps [Gerya, 2022]. During my master thesis research I have focused on developing a numerical model for a subduction zone setting with the long term evolution combined with the short-term seismic cycles. In the last two decades multiple attempts have been made to bridge the gap between the long-term evolution of a subduction plate and the short-term seismic cycle. These models show significant scientific methodological and applied potential, but further development is needed to fully understand the physical mechanisms of a subduction zone.

Van Dinther et al. [2013b] made the first steps by using a continuum visco-elasto-plastic seismo-thermo-mechanical (STM) approach. With this approach they were able to model the long-term evolution of a subducting slab, the short-term seismic cycle and simulate the feedback between them. The model included the three key ingredients for seismic cycle modelling: rate-dependent friction, slow tectonics loading and visco-elastic stress relaxation. Their original model setup was simple and represented an analogue subduction zone model (Fig. 1a). The model setup was extended to a more realistic subduction zone setting symbolizing Southern Chili (Fig. 1b). With this setup they managed to produced simulations with several megathrust earthquakes, which agreed with GPS data of the 2010 M8.8 Maule earthquake [Van Dinther et al., 2013a]. A key problem of this code is the deprivation of an adaptive time stepping and the absence of appropriate time and length scales within the rate-dependent friction formulation [Herrendörfer et al., 2018]. This limits the maximum slip rate and the time step to 5 years during the short-term phase, which makes it impossible

to separate coseismic and early postseismic processes from each other.

Sobolev and Muldashev [2017] also developed a cross-scale model of a subduction zone covering timescales from short- to long-term. Their model setup represents the lithospheric structure of the South Andes (Fig. 2), runs for 10 Myr before switching to the seismic cycle and has a element size of 3 kilometer. In the short-term part elasticity, nonlinear transient viscous rheology, and rate- and state-dependent friction is applied to generate spontaneous earthquake cycles. The maximum time step in the short-term model is 5 years and it decreases to a minimum of 40 seconds in the coseismic period due to adaptive time stepping. They were not able to use the time stepping scheme of Lapusta and Liu [2009] due to a too low grid resolution. Their own adaptive time stepping is based on the amount of strain increase per time step. This introduces small earthquakes and inhibits the simulation of slow-slip events. Critically, it also prevents resolution of rupture nucleation and propagation.
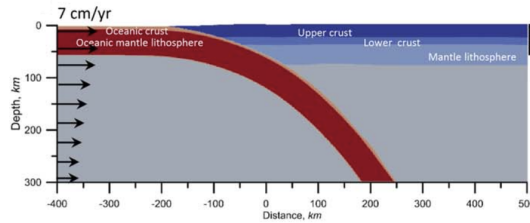


**Figure 2:** Numerical model setup of Sobolev and Muldashev [2017], displaying the spatial distribution of materials and the push velocity.

Van Zelst et al. [2019] modelled the full complexity of the subduction zone by combining two different models. They used the two-dimensional STM model of Van Dinther et al. [2013b] to model 4 million years of subduction and cycles of megathrust events. The fault and surface geometry, fault stress and strength, and heterogeneous material properties at the start of one of the events in the STM model was exported to the dynamic rupture model SeisSol. The event at the dynamic rupture model (DR) had the same characteristics as the STM model, for example the same nucleation location. Only the DR model included more complexity such as various rupture styles and speeds, precursory phases and fault reactivation. The earthquake in the DR model was finished in 80 seconds, had a maximum speed of 10.9 m/s and an average stress drop of 9.3 MPa, while in the STM model the same earthquake lasted 130 years with a maximum speed of $5.7 * 10^{-9}$ m/s and average stress drop of 5.3 MPa.

Dal Zilio et al. [2022] implemented rate- and state-dependent friction in a simple subduction zone setting to investigate how inertia, radiation damping, thermally activated non-linear rheology and off-megathrust splay-faults events affect sequences of seismic and aseismic slip. The setup they used is comparably to the analogue setup of Van Dinther et al. [2013b] (Fig. 1a). The material is non-linear visco-elasto-plastic compressible and the temperature increases with depth, an invariant formulation of the classical rate- and state-dependent friction law is applied and an adaptive time stepping of Lapusta and Liu [2009]. The outcome of their model shows some promising results but should be improved with a more realistic, large-scale setup and by adding a long-term evolution part.
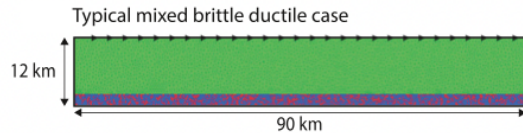


**Figure 3:** Setup of model of Lavier et al. [2021] of a typical mixed brittle ductile case. The green layer is the overriding plate and the layer underneath is the fault zone with the purple material having velocity weakening and the red velocity strengthening behaviour.

Lavier et al. [2021] has examined the physical processes responsible for earthquakes, tremors/SSE's and creep on heterogeneous fault zones. Their model setup is very simplified and exist out of a 2 kilometer

thick horizontal fault zone deformed by a 10 kilometer thick Maxwell visco-elastic overriding plate (Fig. 3). The fault zone exists of a mixture of Maxwell visco-elastic velocity strengthening ductile material and elasto-plastic velocity weakening brittle material. They discovered that simulations with very weak velocity weakening material ($a - b = -0.001$) and strong velocity strengthening material ($a - b = 0.02$) are more likely to exhibit slow slip behavior (Fig. 4). And that at least 50% of the material in the fault zone has to exist out of weakening material for seismic events to occur [Lavier et al., 2021].

Lavier et al. [2021] also examined the difference between very slow SSEs and faster SSEs. During very slow SSEs both brittle and ductile deformation are significantly and the viscosity in the fault zone is highly variable. Zones with low viscosity are slipping while the high viscosity zones are resisting the slip. In the rock record of shear zones the mixed viscous-brittle behaviour is also established [Fagereng et al., 2014]. For fast SSEs the viscosity in the fault zone is persistently low, $10^{17}$ Pa·s, and similar to the viscosity during an earthquake and the deformation is dominated by brittle behaviour.
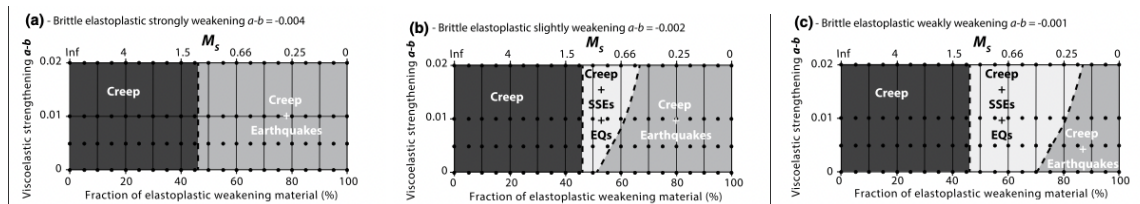


**Figure 4:** Plots of numerical experiments in compositional and frictional parameter space [Lavier et al., 2021]. The Y-axis is the a-b value of the strengthening material and the X-axis the fraction of weakening material on the fault zone. The difference between the a and b value of the weakening material becomes smaller from subplots a to c.

These models have various drawbacks, mostly with reducing the time step to milliseconds in the coseismic period and increasing the slip rate to seismic rates. This prevents the resolution of rupture nucleation and propagation and separating the different phases in the seismic cycle. During my master thesis research I have tried to overcome these by improving the model of a subduction zone setting of Herrendörfer [2018]. For his PhD research Herrendörfer continued with the code of Van Dinther et al. [2013a] and changed the strongly rate-dependent friction to rate- and state-dependent friction for the short-term seismic cycles. He managed to produce earthquakes in a strike-slip setup [Herrendörfer et al., 2018] and slow slip events in a subduction zone setup after 280 Kyr of long-term convergence [Herrendörfer, 2018]. By improving the model I will be the first person to successfully bridge the gap between the long-term evolution with the short-term seismic cycle with the right time scales. Having this code makes it possible to answer long standing questions about the variety of seismicity on the subduction zone and the physical mechanism controlling it. In my guided research I am going to focus on finding the affect of the subducting slab on mantle behaviour and surface displacement. While the focus in my master thesis is on explaining the model with the changes I made and understanding the characteristics and occurrence of megathrust earthquake, slow slip events and steady creep for our STM-RSF model. To validate the model the characteristics will be compare to the outcome of previous research [e.g. Van Dinther et al. [2013a], Van Zelst et al. [2019] and Herrendörfer et al. [2018]].

The outline of this MSc thesis is as followed, in section 3 the whole STM-RSF code is explained and it highlights the changes that have been made during my master thesis research. Section 4 is split up into three different topics namely earthquakes, slow slip events and slip characteristics and model behaviour for different friction parameters. In the earthquake subsection the velocity, stress changes and reflection surfaces will be discussed for one event with a maximum slip rate of 6.3 m/s and duration of 100 seconds. For the slow slip events the occurrence of very slow, $V_p < 10^{-8}$ m/s, and faster, $V_p < 10^{-4}$ m/s, slow slip events are analyzed. The behaviour of our model is dependent on the characteristic slip distance and the ratio between the width of the velocity weakening zone and the nucleation size. For my model the behaviour can be separated into four different regimes, which are comparable to previous studies. Section 5 is split up in two five different topics. In the first and second subsection the characteristics of the simulation containing the reference earthquake is compared to the STM model of Van Dinther et al. [2013a] and the DR model of Van Zelst et al. [2019]. In the third subsection the different regimes of the model behaviour are compared to regimes of Herrendörfer et al. [2018] and Liu and Rice [2007]. The fourth regimes discusses the location of the slow slip events in my model compared to nature. As last the limitations and future work are discussed.

# 3 Method

For my research I adapted the visco-elasto-plastic, continuum mechanics thermomechanical code I2ELVIS [Gerya and Yuen, 2007]. The I2ELVIS code was developed to model long term processes, such as crustal intrusion emplacement of magma's, bending of realistic visco-elasto-plastic plates and core deformation by vigorous shell tectonics activities [Gerya and Yuen, 2007]. The code was extended with a strongly slip-rate dependent friction and inertia by Van Dinther et al. [2013b] and improved by adding a more realistic setup [Van Dinther et al., 2013a]. They were able to simulate slip transients along spontaneous rupture paths, but a limitation of the method is that the coseismic duration, slip velocity and rupture velocity are many orders of magnitude too slow compared to earthquakes in nature [Herrendörfer et al., 2018]. Herrendörfer et al. [2018] continued with the code to try to overcome the limitation of the STM model. They were able to resolve all stages of an earthquake on a strike-slip fault with realistic rupture properties by developing a new invariant formulation of regularized rate- and state-dependent friction [Herrendörfer et al., 2018]. During his PhD research Herrendörfer also added the rate- and state-dependent friction to a subduction zone setup and managed to produce a slow-slip event [Herrendörfer, 2018, Chapter 7]. During my research I used and improved the code of Herrendörfer to produce earthquakes with realistic rupture properties and slow slip events in a subduction zone setting.

## 3.1 Governing equations

For the 2D simulation of geodynamic processes the conservation of momentum and mass are solved to obtain the horizontal- and vertical velocities and pressure [Herrendörfer et al., 2018; Van Dinther et al., 2013b]. The continuity equation assumes conservation of mass on all points,

$$\rho \frac{\partial v_i}{\partial x_i} + \frac{D\rho}{Dt} = 0 \tag{1}$$

where $\rho$ is the density, $\frac{D}{Dt}$ the material time derivative, i and j are coordinate indexes, $v_i$ is the velocity, $x_i$ and $x_j$ are spatial coordinates [Herrendörfer et al., 2018].

The momentum equation is solved for the conservation of momentum in gravity field and under the plain-strain assumption,

$$\frac{\partial \tau_{ij}}{\partial x_j} - \frac{\partial P}{\partial x_j} = \rho \frac{Dv_j}{Dt} - \rho g_i \tag{2}$$

$g_i$ is gravitational acceleration, P is the effective pressure that is defined as $P = P(1 - \lambda)$, where $\lambda$ is the pore fluid ratio and $\tau_{ij}$ is the deviatoric stress tensor, which is defined as

$$\tau_{ij} = \sigma_{ij} + \partial_{ij} P \tag{3}$$

$\sigma_{ij}$ is the Cauchy stress tensor and $\partial_{ij}$ is the Kronecker delta, The density of the material is assumed to be compressible, which causes the density to increase with increasing pressure and depends on the bulk modulus (K) as

$$\frac{D\rho}{Dt} = \frac{\rho}{K} \frac{DP}{Dt} \tag{4}$$

By solving the heat conservation the temperature is provided, the temperature is originally prescribed on the Lagrangian markers and interpolated to Eulerian nodes at the given time instant [Gerya and Yuen, 2003].

$$\rho C_p \frac{DT}{Dt} = -\frac{\partial q_i}{\partial x_i} + H \tag{5}$$

$C_p$ is the heat capacity, q is the heat flux ($q_i = -k \frac{\partial T}{\partial x_i}$) and H are the internal heat sources. The internal heating can include radioactive heating ($H_r$), adiabatic heating ($H_a$) and shear heating ($H_s$). For the simplicity I only included radioactive heating ($H = H_r$).

## 3.2 Rheological equations

To solve the conservation equations (eq. 1 and 2) the stresses in the system are related to velocities via strain rates:

$$\dot{\varepsilon}'_{ij} = \frac{1}{2}\left(\frac{\partial v_i}{\partial x_j} + \frac{\partial v_j}{\partial x_i}\right) \tag{6}$$

The strain rate is decomposed in a viscous, elastic and plastic component.

$$\dot{\varepsilon}'_{ij} = \dot{\varepsilon}'_{ij(viscous)} + \dot{\varepsilon}'_{ij(elastic)} + \dot{\varepsilon}'_{ij(plastic)} \tag{7}$$

The viscous component of the strain rate is controlled by the effective ductile viscosity ($\eta_{eff}$) and the deviatoric stress tensor according to

$$\dot{\varepsilon}'_{ij(viscous)} = \frac{1}{2\eta_{eff}}\tau_{ij} \tag{8}$$

The effective ductile viscosity is represented by a non-linear creep viscosity [Van Dinther et al., 2013a], which is dependent on temperature, pressure and stress according to experimentally determined dislocation creep flow laws as

$$\eta_{eff} = \left(\frac{1}{\tau_{II}}\right)^{(n-1)} \frac{1}{2A_D} \exp\left(\frac{E_a + PV_a}{RT}\right) \tag{9}$$

$n$ is the power law stress exponent, $A_D$ is the pre-exponential factor, $E_a$ is the activation energy, $V_a$ is the activation volume and R is the gas constant. All the variables, except for the gas constant, are dependent on rock type and are given in table 1. Diffusion creep is also present in the model but hardly has an effect on the effective ductile viscosity due to a low threshold value.

The elastic equation assumes proportionality of stress and strain expressed by Hooke's law and is formulated as

$$\dot{\varepsilon}'_{ij(elastic)} = \frac{1}{2G}\frac{D\tau_{ij}}{Dt} \tag{10}$$

where G is the shear modulus.

Traditionally the plastic strain rate is formulated according to the plastic flow law. This classic Coulomb formulation assumes that plastic deformation only occurs if the stress is equal or higher than the plastic yield strength and that the yield strength is dependent on the internal friction [Gerya, 2019; Vermeer and De Borst, 1984]. In the STM-RSF model the non-associated plastic flow law is applied because the material is non-dilatant and compressible [Vermeer and De Borst, 1984; Van Dinther et al., 2013b], which is defined as

$$\dot{\varepsilon}'_{ij(plastic)} = \chi\frac{\partial G}{\partial \tau_{ij}} = \chi\frac{\tau_{ij}}{2\tau_{II}} \tag{11}$$

where $\chi$ is the plastic multiplier, which is an unknown multiplier that makes sure that the deviatoric stress is always equal to the yield stress for the rate- and state-dependent friction [Gerya, 2019]. G is the plastic potential function, which is calculated as follows [Herrendörfer et al., 2018; Vermeer and De Borst, 1984].

$$G = \tau_{II} - \sin(\psi)P - \cos(\psi)C \tag{12}$$

$\psi$ is the dilation angle, this angle represents the ratio of plastic volume changes over plastic shear strain. In all our models we assume that the dilation angle is zero, such that the volume does not change during plastic yielding [Gerya, 2019].

The governing equations are rewritten and discretized in time through an explicit first-order finite-difference scheme. This makes the derivatives of the visco-elastic stresses objective to time and changes the governing equation to [Gerya and Yuen, 2007; Gerya, 2019]

$$\tau_{ij} = 2\eta_{vp}Z\dot{\varepsilon}'_{ij} + t^0_{ij} * (1 - Z) \tag{13}$$

where Z, the visco-elasticity factor, indicates the amount of elastic versus viscous deformation as

$$Z = \frac{G\Delta t}{G\Delta t + \eta_{vp}} \tag{14}$$

The Z-factor changes through time due to the time step and the visco-plastic viscosity, which is defined as [Herrendörfer et al., 2018]

$$\eta_{vp} = \eta_{eff}\frac{\tau_{II}}{2\eta_{eff}\dot{\varepsilon}_{II(plastic)} + \tau_{II}} \tag{15}$$

purely elastic behaviour occurs if Z equals 0, so when $\Delta tG$ is much smaller than $\eta_{vp}$. Viscous behaviour occurs if Z equals 1, so when $\Delta tG$ is larger than $\eta_{vp}$.

### 3.3 Numerical model

The governing equations are solved on a fully staggered Eulerian grid combined with a non-diffusive Lagrangian marker-in-cell technique [Gerya and Yuen, 2007; Gerya, 2019]. With a staggered grid there are two types of nodal points on which different variables are defined and calculated (Fig 5). The shear stress ($\tau_{xy}$), slip rate ($v_p$) and the state variable ($\theta$) are defined in the basic nodal points and the normal stress ($\tau_{xx}$) and pressure (P) are defined in the center nodal points. The visco-plastic viscosity ($\eta_{vp}$) is defined on both nodal points, because it is in both locations needed to be able to solve the Stokes equation. Using this grid makes the discretization of the governing equations natural and gives simple finite differences formulas [Gerya, 2019].
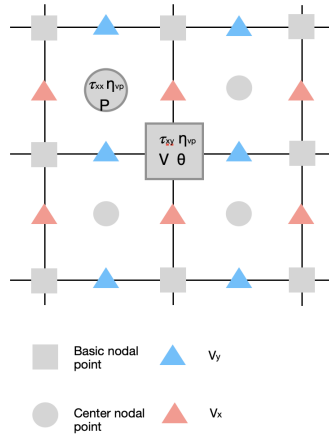


**Figure 5:** Fully staggered 2D numerical grid.

The Eulerian grid is combined with a Langragian marker-in-cell technique to minimize numerical diffusion and to be able to handle large deformation without remeshing [Gerya and Yuen, 2003, 2007; Gerya, 2019]. On the markers, rock type properties are defined and the deviatoric stresses, pressure, velocities, and state variable are stored on it [Herrendörfer et al., 2018]. These are advected through the stationary grid using each time step and velocity. After displacement the rock properties are interpolated back to the nodes using an interpolation scheme, which was updated by Herrendörfer et al. [2018]. The markers are initially randomly distributed and the number of markers increase through time. To fill gaps in the marker distribution in the corners and at shearing zones the optimal interpolation scheme (LinP) is used, which respects the continuity condition and minimizes the local marker density variations [Herrendörfer, 2018].

The top layer of the model consists of sticky air, which is a layer with a low density and low viscosity such that it operates as an internal free surface [Gerya, 2019]. The density is similar to the density of air, but

the viscosity is higher than the viscosity of water to avoid numerical issues that appear when the magnitude difference is larger than 3 orders of magnitude compared to the mantle. The viscosity of the sticky air changes according to the time step, such that it always behaves viscous and deforms at very low stresses [Gerya, 2019]. The viscosity of the sticky air is set as

$$\eta_{air} = G_{air} * \frac{\Delta t}{1e2} \tag{16}$$

with $G_{air}$ is 700GPa.

The left and right boundaries are free slip, which requires that the normal velocity component on the boundary is zero and the two other components do not change across the boundary [Gerya, 2019]. The lower boundary is vertically penetrable and external free slip is satisfied at a depth of 500 kilometer.

## 3.4  Drucker-Prager plasticity

A STM simulation consist out of two parts. The long-term for which the governing equations are solved with regular Drucker-Prager plasticity [Gerya and Yuen, 2007] and the short-term that solves for rate- and state-dependent friction. In regular Drucker-Prager plasticity, plastic deformation only occurs if the second invariant of the stress is higher than a pressure dependent yield strength ($\sigma_{yield}$) [Vermeer and De Borst, 1984; Van Dinther et al., 2013b; Gerya, 2019]

$$
\begin{aligned}
\text{for } \sigma_{II} &< \sigma_{yield} \\
\dot{\varepsilon}_{ij(plastic)} &= 0 \\
\text{for } \sigma_{II} &= \sigma_{yield} \\
\dot{\varepsilon}_{ij(plastic)} &= \chi \frac{\tau_{ij}}{2\tau_{II}}
\end{aligned} \tag{17}
$$

The yield strength, $\sigma_{yield}$ is defined as

$$\sigma_{yield} = P\mu_0 + C \tag{18}$$

where $\mu_0$ is the internal friction coefficient, $C$ the cohesion and P the effective pressure, which is calculated as $P = -(\sigma_{xx} + \sigma_{yy} + \sigma_{zz}/3)$.

The transition from the long term solution to the short-term occurs by gradually decreasing the time step from 95 years to 116 days and by calculating the equilibrium value of the state parameter ($\Theta$), defined as

$$\Theta = \frac{a \log\left(\frac{2V_0}{V_p} \sinh\left(\frac{\mu}{a}\right) - \mu\right)}{b} \tag{19}$$

The equilibrium value is determined for each time step in the long term model and is used to start the iterations with the rate- and state-dependent friction [Gerya, 2019].

## 3.5  Invariant reformulation of the regularized rate and state friction

In most classical earthquake cycle simulations, slip on a fault is governed by rate- and state-dependent friction, which allows to resolve every aspect of the earthquake cycle [Barbot et al., 2012]. "Slide-hold slide" and "velocity stepping" laboratory rock experiments form the experimental basis of the rate- and state-dependent friction formulation [Dieterich, 1972], defined as

$$\tau_s = \mu\sigma_n = \left[\mu_0 + aln\left(\frac{V}{V_0}\right) + bln\left(\frac{\Theta V_0}{L}\right)\right]\sigma_n \tag{20}$$

the shear stress ($\tau_s$) is calculated as a function of the normal stress ($\sigma_n$), the direct effect ($aln(\frac{V}{V_0})$) and the evolution effect ($bln(\frac{\Theta V_0}{L})$). The friction is velocity weakening if the evolution effect is greater than the direct effect ($b > a$), which means that instabilities can grow to a point where an earthquake can occur (Fig. 6). The friction is velocity strengthening if the direct effect is greater than the evolution effect ($b < a$), which

means that instabilities will decay without causing an earthquake. L is the characteristic slip distance, which correlates with the roughness of the frictional surface and the particle size of the gouge along the surface [Dieterich et al., 1981].
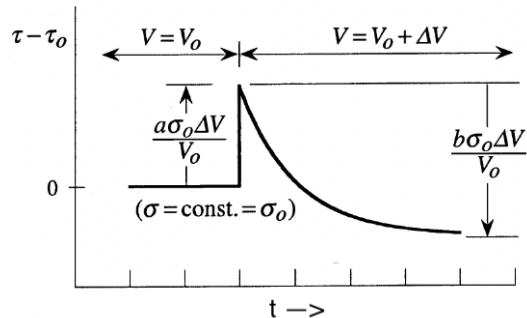


**Figure 6:** Change in shear stress through time of a velocity weakening material for a fixed normal stress, adapted from Rice et al. [2001].

Over the years there have been some physical interpretations of the terms in equation 20, which has led to the regularized version of the rate and state-dependent friction [Rice et al., 2001]

$$\tau_s = arcsinh \left[ \frac{V}{2V_0} exp \left( \frac{\mu_0 + bln(\frac{\Theta V_0}{L})}{a} \right) \right] a\sigma_n \tag{21}$$

Herrendörfer et al. [2018] made three changes to relate the rate- and state-dependent friction formulation of equation 21 and the yield condition used in the continuum approach. The first difference is how deformation is defined. In the classical formulation slip occurs along a predefined fault plane. In the continuum approach plastic deformation is treated as strain, which can occur everywhere and can spontaneously localize into a shear zone or fault zone of finite thickness [Gerya, 2019]. This requires the slip rate magnitude ($v_p$) to be related to the second plastic strain rate invariant ($\dot{\varepsilon}'_{II(plastic)}$), which is done by using the fault zone thickness (D) as scaling factor [Van Dinther et al., 2013b; Herrendörfer et al., 2018].

$$V_p = 2\dot{\varepsilon}'_{II(plastic)}D \tag{22}$$

The second difference is how the fault strength is assessed. The classical formulation uses shear stress and normal stress to calculate the shear strength. These are both related to the orientation of the predefined fault. In the continuum approach scalars are used that are invariant to the coordinate system and are thus able to adapt to spontaneous fault evolution [Gerya, 2019]. To overcome this the mean stress and second stress invariant are used instead of normal and shear stress [Herrendörfer et al., 2018]. The pressure is defined as the negative of the mean stress ($P = -(\sigma_{xx} + \sigma_{yy} + \sigma_{zz}/3)$) and is positive under compression [Gerya, 2019].

The third difference is when slip occurs. For the yield condition used in the continuum approach, plastic deformation only occurs if the second invariant of the deviatoric stress tensor is equal to or larger than the yield strength and it stops if the stress falls below it [Herrendörfer et al., 2018]. In contrast, in the RSF equation it is assured that slip always occurs if the shear stress is larger than zero. However slip only becomes noticeable when the stress reaches an interface strength, which was noted by Nakatani [2001]. They defined the interface strength equal to the term $\sigma_n \left[ \mu_0 + b \ln \left( \frac{\Theta V_0}{L} \right) \right]$ in equation 20. Following Nakatani [2001] the rate- and state-dependent friction can be regarded as a smooth version of the classical yield strength and the smoothness is proportional to $a$. If $a$ is zero the rate- and state-dependent friction approaches the classical yield strength [Herrendörfer et al., 2018].

By applying the three improvements and by taking the classical formulation of the yield strength into account the following equation is defined

$$\tau_{II} = \sigma_{yield} = C + \arcsin \left[ \frac{V_p}{2V_0} \exp \left( \frac{b}{a} \ln \left( \frac{\Theta V_0}{L} \right) + \frac{\mu_0}{a} \right) \right] aP \tag{23}$$

9

The second invariant of the deviatoric stress ($\tau_{II}$) depends on the plastic slip rate ($V_p$) and the evolving state variable ($\Theta$), which is calculated with the aging evolution law: $\frac{\partial \Theta}{\partial t} = 1 - \frac{V_p \Theta}{L}$. The law has experimental support and partial theoretical justification [Dal Zilio et al., 2022], but the formulation that best describes the evolution of the state variable for various laboratory experiments is still a topic of ongoing research [Dal Zilio et al., 2022].

Equation 23 implies that $\tau_{II} = \sigma_{yield}$, which means that the yielding condition is always fulfilled and some plastic slip always occurs [Herrendörfer et al., 2018]. The interface yield strength is based on Nakatani [2001] and defined as

$$\sigma_{yield}^{RSF} = P\left[\mu_0 + bln\left(\frac{\Theta V_0}{L}\right)\right].$$ (24)

In the code the dimensionless state parameter ($\Omega = \ln\frac{\theta V_0}{L}$) is computed by using an analytical solution derived by Lapusta and Liu [2009] under the assumption of constant plastic slip during one time step [Gerya, 2019]

$$\Omega_{(i,j)} = \ln\left[\exp(\Omega_{0(i,j)}\left(1 - \frac{V_{p(i,j)}\Delta t}{L_{(i,j)}}\right) + \frac{V_0 \Delta t}{L_{(i,j)}}\right] \qquad \begin{array}{l} if\frac{V_p \Delta t}{L_{(i,j)}} \leq 10^{-6} \\[3pt] \\ if\frac{V_p \Delta t}{L_{(i,j)}} > 10^{-6} \end{array}$$ (25)

$$\Omega = \ln\left[\frac{V_0}{V_{p(i,j)}} + \left(\exp(\Omega_{0(i,j)}) - \frac{V_0}{V_{p(i,j)}}\right)\exp\left(-\frac{V_{p(i,j)}\Delta t}{L_{(i,j)}}\right)\right]$$ (26)

## 3.6 Adaptive time step

An adaptive time stepping is used to obtain time steps in the order of milliseconds in the coseismic period and in the order of days in the interseismic. The adaptive time stepping scheme used in our model is constructed by Herrendörfer et al. [2018] and is based on the requirement that the length of the time step is the minimum of the time steps needed to resolve the state weakening (w) and healing (h), to limit the displacement per grid cell (d) and the visco-elasto-plastic relaxation time scale (vep),

$$\Delta t = \zeta min_{n_x=1,n_y=1}^{N_x,N_y}\left[min\left[\Delta t_w, \Delta t_h, \Delta t_d, \Delta_{vep}\right]\right]$$ (27)

where $\theta$ is the time step factor that is set to to 1.0 according to Herrendörfer et al. [2018]. A time step factor smaller than 1 leads to a higher computational cost due to the increases amount of time steps needed and a factor larger than 1 leads to a higher number of Picard iterations and time step corrections [Herrendörfer et al., 2018].

The adaptive time step developed by Lapusta et al. [2000] is used to resolve the minimum time step for the state weakening and is defined as,

$$\Delta t_w = \Delta \theta_{max}\frac{L}{V_p}$$ (28)

it is dependent on the coefficient, $\Delta\theta_{max}$, which is limited to a maximum value of 0.2. The coefficient is a function of a, b, L, P, G and the grid size, $\Delta x$, and defined as,

$$\xi = \frac{1}{4}\left[\frac{kL}{aP} - \frac{b-a}{a}\right]^2 - \frac{kL}{aP}$$ (29)

if $\xi > 0$:

$$\Delta\theta_{max} = min\left[\frac{aP}{kL - (b - a_P)}, 0.2\right]$$ (30)

if $\xi < 0$:

$$\Delta\theta_{max} = min\left[1 - \frac{(b-aP)}{kL}, 0.2\right] \tag{31}$$

with $k = \frac{2}{\pi}\frac{G^*}{\delta x}$ being the stiffness of a system assuming uniform slip per cell. If the stiffness is smaller than a critical value any perturbation will grow and the cell behaves with steady state velocity weakening behaviour [Lapusta et al., 2000]. I put a limit on the weakening time step for small slip rates, to make sure the model has a smooth transition from inter- to coseismic time steps. The minimum slip rate for which the weakening time step is calculated is equal to $10^{-3}$ m/s. Lapusta and Liu [2009] use the adaptive time stepping scheme of Lapusta et al. [2000] and also add a minimum time to have a good resolution of dynamic rupture propagation.

The minimum time step for the state healing is determined by taking a fraction of the evolving state parameter ($\theta$),

$$\Delta t_h = 0.2\theta \tag{32}$$

the fraction limits the time step, such that the time step during the initial loading phase is not too large. The fraction is chosen according to the $\Delta t_{max}$ for the state weakening time step [Herrendörfer et al., 2018].

The displacement per time step is limited to a fraction of the grid size

$$\Delta t_d = \Delta d_{max}min\left[|\frac{\Delta x}{v_x}|, |\frac{\Delta x}{v_y}|\right] \tag{33}$$

$\Delta d_{max}$ is set to 0.02 according to Herrendörfer et al. [2018].

Herrendörfer et al. [2018] added the visco-elasto-plastic relaxation time scale, because the adaptive time step developed by Lapusta et al. [2000] was not sufficient if the friction is not influenced by the evolution effect, i.e. when viscous deformation dominates. The visco-elasto-plastic relaxation time scale combines the visco-elastic relaxation time scale and the elasto-plastic time scale through the value of $f_{max}$

$$\Delta t_{vep} = f_{max}\frac{\eta_{vep}}{G} \tag{34}$$

$f_{max}$ is set to 0.2 according to Herrendörfer et al. [2018].

## 3.7 Solution cycle

The structure of the solution cycle used for the long-term part with Drucker-Prager plasticity is the same as for the short-term part with rate- and state-dependent friction (Fig. 7). Highlighted in grey is the iteration solution cycle to solve the momentum and continuity equations, which uses predictor-corrector Picard iterations shown in brown [Herrendörfer et al., 2018]. The iteration starts by determining the initial time step (Eq. 27), which is based on the the solution of the previous time step.

The stress and strain rate are calculated with the outcome of the momentum and continuity equations. The strain rate is dependent on the x- and y-velocity.

$$\dot{\varepsilon}_{xx} = \frac{1}{2}\left(\frac{\delta Vx}{\delta X} - \frac{\delta Vy}{\delta Y}\right)$$
$$\dot{\varepsilon}_{xy} = \frac{1}{2}\left(\frac{\delta Vx}{\delta Y} - \frac{\delta Vy}{\delta Y}\right) \tag{35}$$

The stress is dependent on the stress of the previous time step ($\sigma_0$), the effective ductile viscosity ($\eta_{eff}$) and the Z-value.

$$\sigma_{xx} = 2.0 * \eta_{eff} * \dot{\varepsilon}_{xx} + \sigma_0 * (1 - Z)$$
$$\sigma_{xy} = 2.0 * \eta_{eff} * \dot{\varepsilon}_{xy} + \sigma_0 * (1 - Z) \tag{36}$$

With $\sigma_{xx}$ and $\sigma_{xy}$ the second invariant of the deviatoric stress is calculated, which is used for the plastic slip rate. In the long-term phase plastic slip only occurs if the yield strength is reached (Eq. 17, 18) and calculated as followed
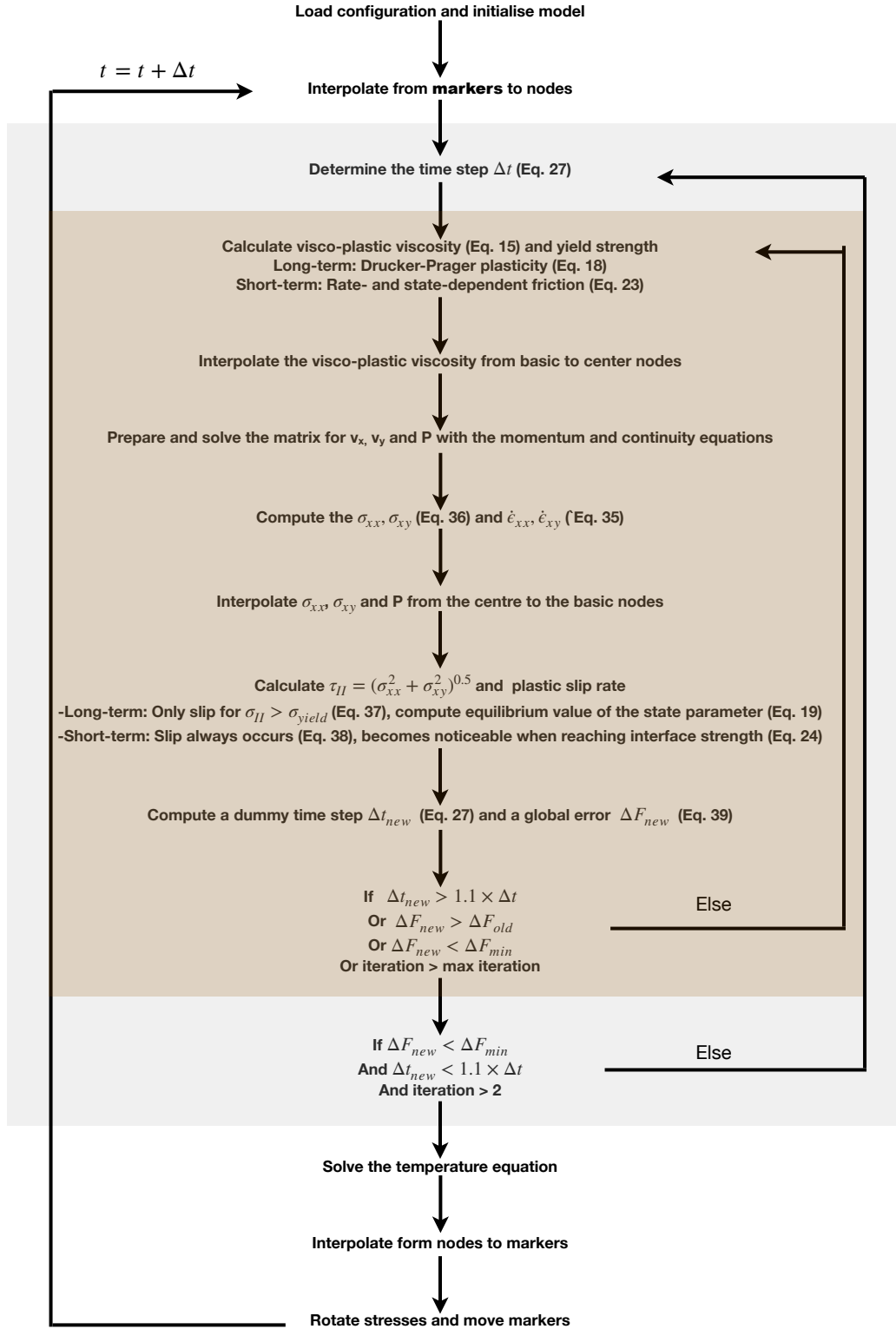
**Load configuration and initialise model**

$t = t + \Delta t$

**Interpolate from markers to nodes**

**Determine the time step $\Delta t$ (Eq. 27)**

**Calculate visco-plastic viscosity (Eq. 15) and yield strength**
**Long-term: Drucker-Prager plasticity (Eq. 18)**
**Short-term: Rate- and state-dependent friction (Eq. 23)**

**Interpolate the visco-plastic viscosity from basic to center nodes**

**Prepare and solve the matrix for v$_x$, v$_y$ and P with the momentum and continuity equations**

**Compute the $\sigma_{xx}, \sigma_{xy}$ (Eq. 36) and $\dot{e}_{xx}, \dot{e}_{xy}$ (Eq. 35)**

**Interpolate $\sigma_{xx}, \sigma_{xy}$ and P from the centre to the basic nodes**

**Calculate $\tau_{II} = (\sigma_{xx}^2 + \sigma_{xy}^2)^{0.5}$ and plastic slip rate**
**-Long-term: Only slip for $\sigma_{II} > \sigma_{yield}$ (Eq. 37), compute equilibrium value of the state parameter (Eq. 19)**
**-Short-term: Slip always occurs (Eq. 38), becomes noticeable when reaching interface strength (Eq. 24)**

**Compute a dummy time step $\Delta t_{new}$ (Eq. 27) and a global error $\Delta F_{new}$ (Eq. 39)**

**If $\Delta t_{new} > 1.1 \times \Delta t$**
**Or $\Delta F_{new} > \Delta F_{old}$**
**Or $\Delta F_{new} < \Delta F_{min}$**
**Or iteration > max iteration**

Else

**If $\Delta F_{new} < \Delta F_{min}$**
**And $\Delta t_{new} < 1.1 \times \Delta t$**
**And iteration > 2**

Else

**Solve the temperature equation**

**Interpolate form nodes to markers**

**Rotate stresses and move markers**

**Figure 7:** Solution cycle, grey is the iteration solution cycle to solve the momentum and continuity equations and Picard-iterations steps are in brown.

$$V_p = D * \left( \frac{\tau_{II}}{2} * (\frac{1}{\eta_p} - \frac{1}{\eta}) \right) \tag{37}$$

$$\text{with } \eta_p = \frac{\sigma_{yield}}{E2EL}$$

$$\text{with } E2EL = \frac{\tau_{II}}{\frac{\eta_{vp}}{G*dt - \eta_{vp}}}$$

D is the fault width, which is calculated as $D = 2 * 0.5(g_x + g_y)$.
The plastic slip rate for rate- and state-dependent friction is computed as followed

$$V_p = 2V_0 arcsin \left( \frac{4max(\tau_{II} - C)}{aP} \right) \exp \left( -\frac{b\Omega + \mu_0}{a} \right) \tag{38}$$

$V_0$ is a predefined value equal to $4 * 10^{-9}$ m/s.

One of the last step is calculating the global error $\Delta F$, this is the difference between the yield strength, $\sigma_{yield}$, and the second invariant of the deviatoric stress, $\tau_{II}$, taken for each basic node and divided by the total number of basic nodes, N.

$$\Delta F = \left( \frac{\sigma_{yield} - \tau_{II}}{N} \right)^2 \tag{39}$$

If the error value is higher than the previous error value and the number of iteration cycles is equal or higher than 5 a new time step is determined. Next to the global error there is a dummy time step determined with the new parameter values. If this dummy values changes with 10% towards the initial time step, a new time step is used for the next iteration. If the above mentioned statements are not true the code checks if the $\Delta F$ is smaller than the minimum value, which is allocated in the mode file and differs through time.

When the iteration solution cycle is completed the properties are interpolated to markers. After interpolation the markers are moved through the grid for the calculated time step and velocity and the stresses are rotated.

## 3.8 Model setup
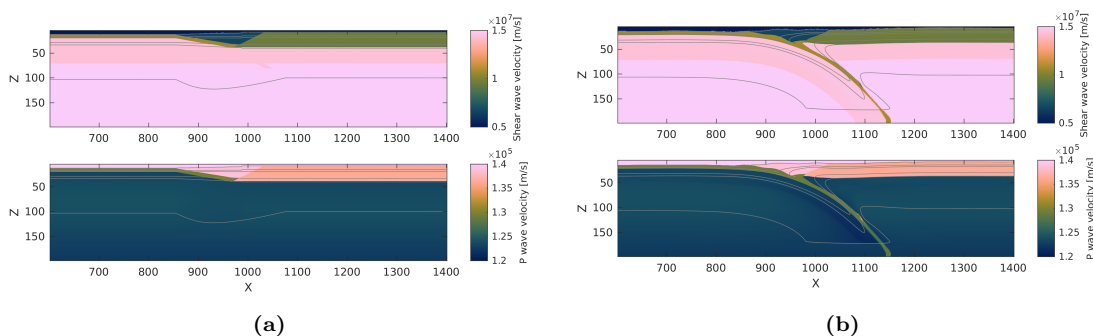


**Figure 8:** (a) Impedance of initial setup and (b) after 4 Myr of subduction for shear wave (top) and for P-wave (bottom). The shear wave velocity is calculated with the density and the shear modulus ($Sv = (G * \rho)^{0.5}$) and the P-wave velocity is calculated with the bulk modulus ($Pv = (\frac{B + 1.3G}{\rho})^{0.5}$).

The model setup is the adopted from Van Dinther et al. [2013a] (Fig. 1b), the model is a $1500 \times 200 km^2$ trench-normal section of the Southern Chilean convergent margin. At this margin the oceanic Nazca plate subducts into the upper mantle beneath the continental South American plate. The oceanic plate moves at a velocity of 7.5 cm/yr, due to an imposed push 500 kilometer seaward of the trench [Van Dinther et al., 2013a; van Dinther et al., 2014]. The subduction zone is initiated by an initial weak zone, which has a wet olivine flow law and a very low plastic strength. The weak zone is replaced by oceanic crust when the slab

reaches an age of 3.5 Myr. At a depth of 170 kilometers the slab is cut off and the temperature below is equal to 1412°C. From here on I identify rocktype using the impedance (Fig 8), because in our model the rocktype is only saved on the markers making it impossible to recreate figure 1. After four million years of subduction the rate- and state-dependent friction is initiated (Fig. 8b).

Seven different rock types are used to realistically model a subduction zone [Van Dinther et al., 2013a]. The oceanic crust consist out of a 5 kilometer thick gabbro layer overlain by 2 kilometer of fractured and hydrated oceanic upper crust. This layer approximates the subduction channel with subducted sediments and potential continental crust slices. The values for the material parameters for each rock type are shown in table 1. The parameters comply with data set used in the study of Van Zelst et al. [2019], which has updated values for $\mu_s$ and $G$ compared to the data set of Van Dinther et al. [2013b]. In contrast to van Dinther et al. [2014] we do not account for sedimentation, erosion, and fluid and hydration processes.

During the short-term phase rate- and state-dependent friction is only applied to a part of the whole domain. The horizontal domain is between 800 and 1250 kilometer and the vertical domain is everything lower than 13.5 kilometer. This is done to make sure that the vertical boundaries and the sticky air do not effect the solution of the model.
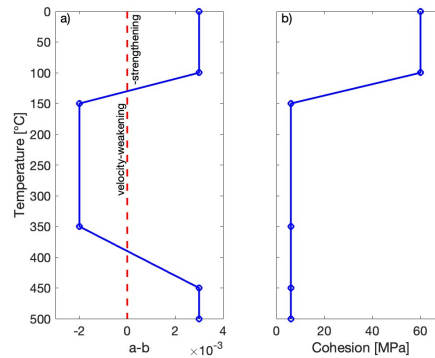


**Figure 9:** a) Profile of direct effect, a, minus the evolution effect, b, along the fault rock with temperate. b) Profile of cohesion along the fault rock with temperate.

The fractured oceanic upper crust, called fault rock from now on, features temperature dependent RSF parameters deducted from laboratory experiments on simulated illite-quartz fault gouge [Den Hartog et al., 2012]. In the velocity weakening domain the evolution effect is greater than the direct effect, which means that instabilities can grow to a point where an earthquake can occur. The velocity weakening domain is surrounded by an updip and downdip domain with velocity strengthening. Between the domains the RSF parameters (a-b) have a linear change (Fig. 9a). All other rock types are velocity strengthening, which means that the direct effect is larger than the evolution effect and instabilities will decay without causing an earthquake. For the long-term the cohesion is 6 MPa in every rocktype, but for the short-term the cohesion increases to 200 MPa for every rocktype except on the faultrock. By increasing the cohesion on every rock type except on the fault rock we make sure that faulting is localised on the fault zone. The cohesion on the faultrock changes with temperature and has the same updip transition as the velocity weakening domain (Fig. 9b). The pore fluid ratio, $\lambda$, is set to 0.95 for the fault rock. This value is suggested by [Van Dinther et al., 2013a] and is supported by the differential stress predictions for the Southern Chilean margin [Seno, 2009]. The pore fluid ratio is equal to 0.7 for the upper crustal rocktypes and equal to 0.4 for the other rocktypes

The changes I made during my master thesis research are: Increased the long-term part from 280 Kyr to 4 Myr, Adjusted the viscosity at the boundaries, Modified how cohesion was added to the invariant formulation of RSF, Removed the initial weak zone, Changed the value of the cohesion and the pore fluid ratio, Added the temperature dependent velocity weakening, Limited the weakening time step and Restricted the domain where the rate- and state-dependent friction is used. I also altered the plotting methods used by Van Dinther et al. [2013a] to fit the new model. There are also some changes that were made, which are not in the STM-RSF model right now. These still induced some instabilities, which can be fixed with limited effort. One example is the thinning of the oceanic crust at the left side that occurs in the model right now. This

| Material | Flow Law | $\eta_0$ $Pa^n s$ | n $-$ | $E_a$ $J/mol$ | $V_a$ $J/bar$ | G $GPa$ | $\rho_0^d$ $kg/m^3$ | $H_r$ $\mu W/m^3$ | $\mu$ $-$ |
|---|---|---|---|---|---|---|---|---|---|
| Sediments(4) | Wet quartzite | $1.97 * 10^{17}$ | 2.3 | $1.54 * 10^5$ | 0.8 | 17 | 2600 | 2 | 0.35 |
| Upper cont. crust(5) | Wet quartzite | $1.97 * 10^{17}$ | 2.3 | $1.54 * 10^5$ | 1.2 | 34 | 2700 | 1 | 0.72 |
| Lower cont. crust(6) | Wet quartzite | $1.97 * 10^{17}$ | 2.3 | $1.54 * 10^5$ | 1.2 | 34 | 2700 | 1 | 0.72 |
| Upper oceanic crust(7) | Wet quartzite | $1.97 * 10^{17}$ | 2.3 | $1.54 * 10^5$ | 0.8 | 38 | 3000 | 0.25 | 0.5 |
| Lower oceanic crust(8) | Plagioclase | $4.80 * 10^{22}$ | 3.2 | $2.38 * 10^5$ | 0.8 | 38 | 3000 | 0.25 | 0.85 |
| Lithospheric mantle(9) | Dry olivine | $3.98 * 10^{16}$ | 3.5 | $5.32 * 10^5$ | 0.8 | 6.3 | 3300 | 0.022 | 0.6 |
| Mantle(10) | Dry olivine | $3.98 * 10^{16}$ | 3.5 | $5.32 * 10^5$ | 0.8 | 7.2 | 3300 | 0.022 | 0.6 |

**Table 1:** Material parameters, see Van Zelst et al. [2019] for more explanation and references.

happens due to the landward speed of the plate and no formation of new crust. To prevent this a few lines of code have been added and has proven to work on the long term part. It will not change the results, because the rate- and state-dependent friction is not calculated in that part of the model.

# 4    Results and Analysis

The result section is divided into three main parts. In the first part I study a simulation with a fast earthquake. The second part discusses a simulation with many slow slip events and the last part describes the model behaviour for changes in the friction parameters.

## 4.1    Fast earthquake

### 4.1.1    Loading of the megathrust

I managed to fully bridge all relevant time scales from millions of years down to milliseconds, such that nucleation, propagation and arrest of an earthquake can be resolved for the first time. Before the transition to RSF the oceanic plate moves with 7.5 cm/yr towards the continental plate, from 950 kilometer the horizontal movement decreases and the plate tarts to subduct into the mantle (Fig. 10a). The continental plate has almost no movement except for in the mantle with temperatures higher than 1300°C. Here the mantle moves upward, counteracting the downward movement of the slab (Fig. 10a). After the transition to rate- and state-dependent friction there is an initial loading phase in which the model finds a new balance. The velocities in the continental and oceanic plate are changed compared to the long-term when the new balance is established in the short-term phase (Fig. 10b). The horizontal velocity increases in the subducting plate towards the continental plate to velocities higher than 18 cm/yr. This is 2 times larger than the push velocity, which is not changed after the transition. The seismogenic zone moves with a lower speed than the rest of the subducting plate causing a slip deficit and a potential location for the nucleation of an earthquake (Fig. 10b). The continental plate starts to move with a speed of 18 cm/yr due to the landward push of the subducting plate. Between 950 and 1030 kilometer the horizontal velocity is lowered to 17 cm/yr due to the reduction of movement at the fault zone. Both the continental and subducting plate move upwards until 1150 kilometer, after which it switches to downward (Fig. 10b).

The increase in speed of the subducting plate and the upward movement are caused by the mantle moving upwards underneath the slab. The downward movement of the mantle into the lower boundary from 1150 kilometer is linked to the upward movement by mass driven return flow. At this moment I am not sure whether the downward movement causes the upward flow or vice versa, but I am certain that both problems are caused by the lower boundary condition. A more detailed description of the problems in the interseismic period and possible solutions can be found in the discussion section of this paper. Nonetheless, locking and loading occurs and earthquakes can nucleate in the simulations.

There is a change in visco-elasticity factor (Eq. 14) from the long-term phase to the interseismic and the coseismic period (Fig. 11). During the long-term the fault rock has a Z-factor of approximately 0.5 with a fast increase to 1 for temperatures higher than 450°C due to the brittle-ductile boundary (Fig. 11b). The mantle below 1300°C also behaves in a viscous matter, while the rest of the mantle behaves purely elastic.
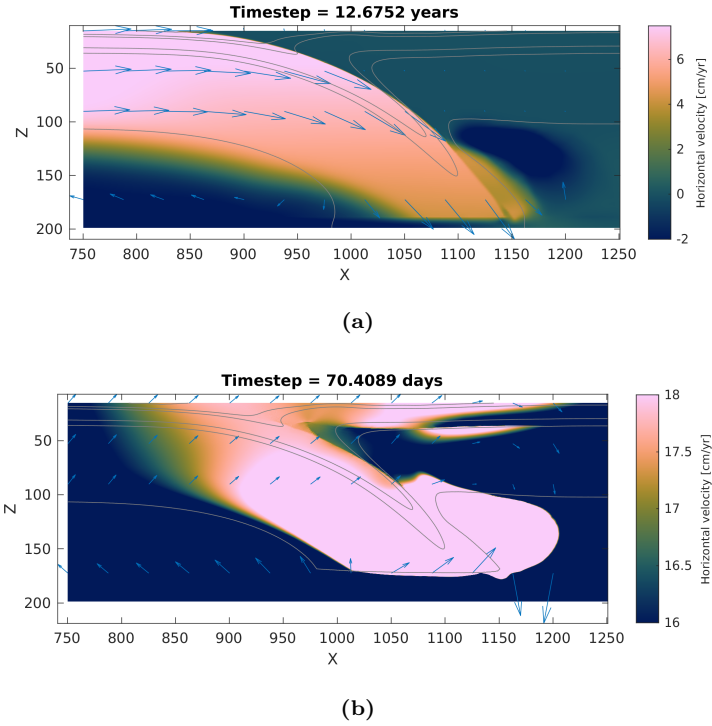
**(a)**



**(b)**

**Figure 10:** Velocity arrows plotted over the horizontal velocity in the long-term phase (a) and in the interseismic period 24 years before the reference earthquake (b).

The lower continental crust has a viscous behaviour for higher temperatures due the temperature dependence of non-linear creep (Fig. 11a) . In the interseismic period, 24 years before the earthquake, almost the whole domain behaves purely elastic except for the fault rock with temperatures higher than 450°C, the mantle underneath the subducting slab and the mantle wedge (Fig. 11b). The behaviour changes to purely elastic everywhere during the coseismic period due to the small time step (Fig. 11c).



**(a)**



**(b)**



**(c)**
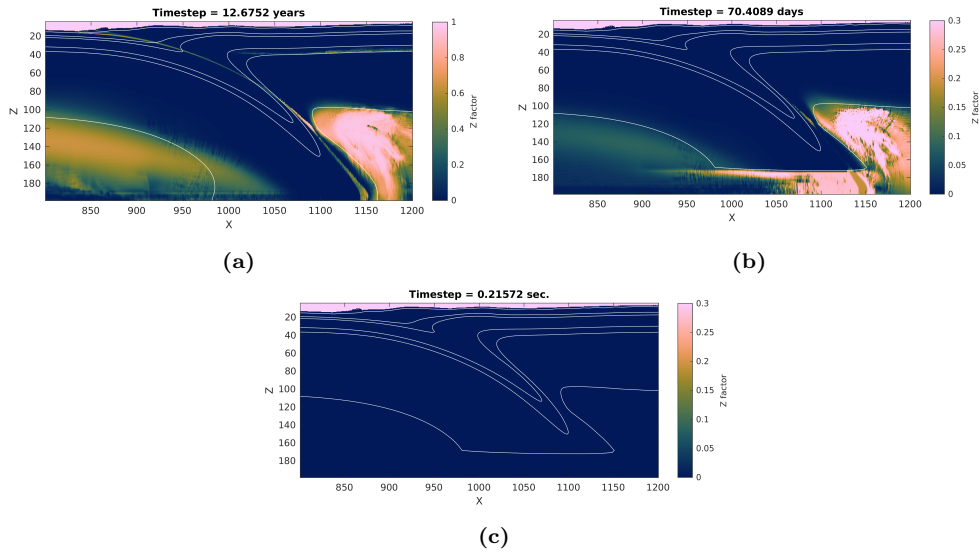
**Figure 11:** Visco-elasticity factor, Z, for the long-term phase (a), the interseismic (b) and the coseismic period (c).

### 4.1.2 Reference simulation
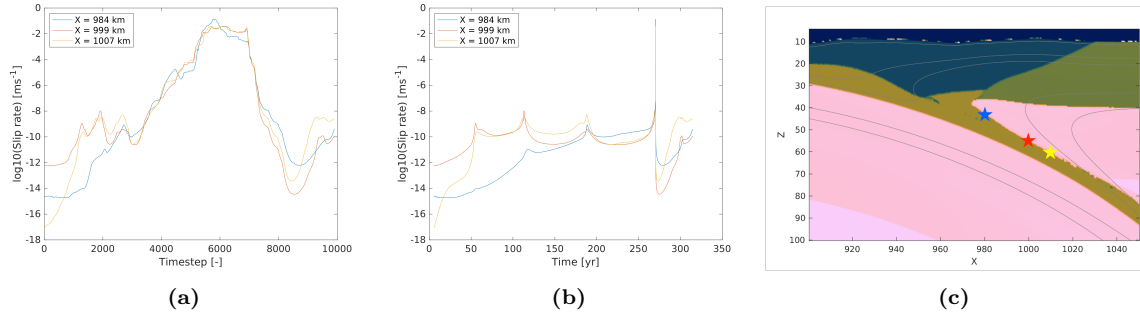


**Figure 12:** Slip rate at three different locations on the fault zone with (a) time step and (b) absolute time on the x-axis. The plot starts (t=0) when the initial loading phase is completed and a new equilibrium is set. c) Location of the three points overlain by the S-wave impedance and the isotherms in grey.

For the analysis of the nucleation, propagation and arrest of an earthquake the simulation with a value of 0.012 for the direct effect, 0.02 for the evolution effect and a value of 0.07 for the characteristic slip distance in the seismogenic zone is studied. This reference model features two slow slip events and one earthquake (Fig 12). The absolute time of the earthquakes is close to 100 seconds and it is preceded by a fore-shock 24 minutes before the main earthquake. The main earthquake is resolved in 1500 time steps, due to the adaptive time stepping scheme. The time step decreases from 72 days during the interseismic period to milliseconds in the coseismic period with a minimum value of $4.0*10^{-3}$ seconds. During the coseismic period the controlling time step is the healing time step and for the interseismic it is the weakening time step.

After the main earthquake is completed small oscillations develop, which decay into stable sliding. The maximum slip rate during the earthquake is 6.32 m/s at depth of 58 kilometer, which is much larger than the seismic threshold value of 0.17 m/s as defined by Rubin and Ampuero [2005]:

$$V_{thres} = \frac{2aPC_s}{G} \tag{40}$$

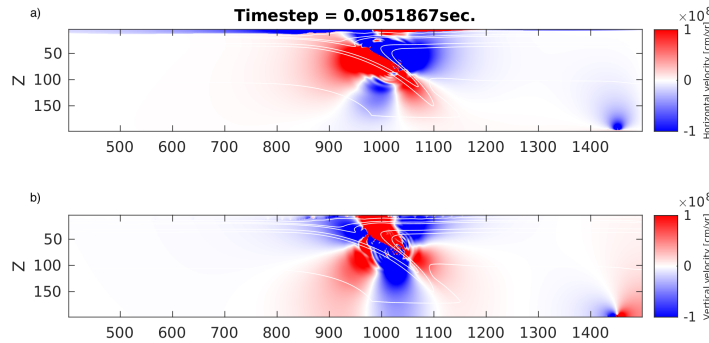$C_s$ is the shear speed wave and equal to 3300 m/s.



**Figure 13:** a) Horizontal and (b) vertical velocity for a simulations with a direct effect of 0.11, evolution effect of 0.22 and characteristic slip distance of 0.08 just before it quits.

There are multiples models with higher maximum slip rates, with the highest being 19 m/s. In these simulations reflections occur near the lower right corner, that causes the velocity to increase locally (Fig. 13). The movement at the lower right boundary disturbs the propagation of the earthquake and eventually leads to failure of the simulations before the postseismic phase is reached. I think that the reflection is arising due a lower boundary condition problem as the upward movement in the interseismic period (Fig. 10b). For my master thesis a whole earthquake cycle was preferred, therefore the analysis is done with the model with a

17

maximum slip rate of 6.3 m/s and no reflections at the lower right boundary. This is still very high and a larger earthquake is not needed for the scope of this research.

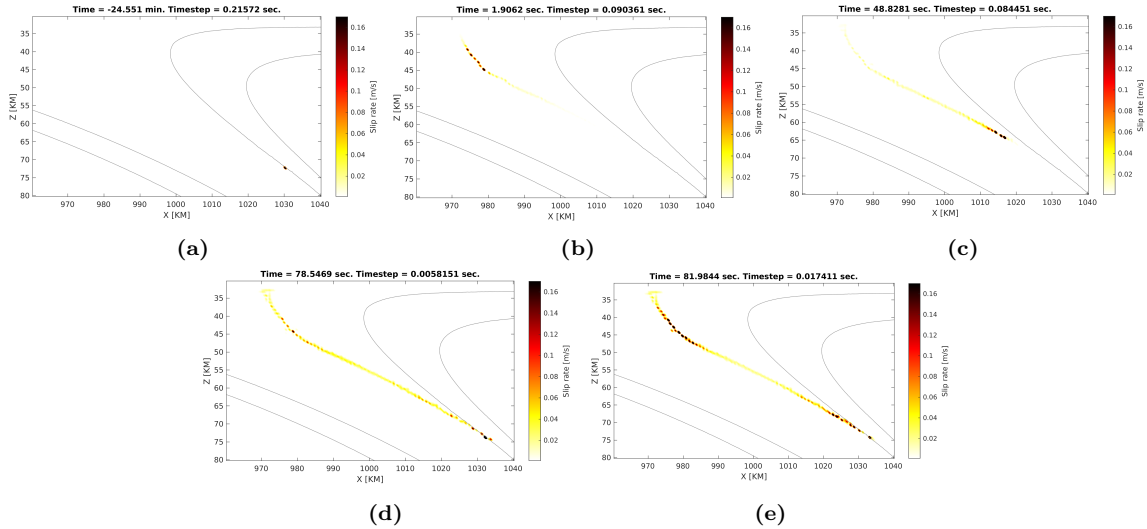### 4.1.3 Rupture propagation and reflection surfaces



**Figure 15:** Slip rate (a) at fore-shock, (b) at nucleation of main earthquake, (c) after 48.8 seconds, (d) after 78.5 seconds and (e) after 82.0 seconds. Time equal zero is the moment the slip rates reach the seismic threshold at the nucleation of the main shock.

Before the main earthquake starts there is a fore-shock at the downdip limit of the seismogenic zone. The slip is very locally increased to values of 1.6 m/s at a depth of 60 kilometers for a time span of 2.2 seconds (Fig. 14a, 15a). After the fore-shock the slip velocity decrease to sub-seismic slip rates, while propagating upwards along the megathrust (Fig. 16a). The main earthquake nucleates at a depth of 30 kilometers, 24 minutes after the fore-shock (Fig. 14b and 15b). At this depth the path of the rupture becomes more vertical into the sedimentary wedge. At the bottom of the sedimentary wedge fault rock is located, which is scrapped off the down going plate during the long term subduction (Fig. 8b). From here the nucleation propagates upwards until the sediment basalt boundary is reached and downwards along the megathrust. Near the downdip limit of the seismogenic zone the nodes that already have slipped during the fore-shock are reactivated and seismic waves start to emit from the lower boundary of the seismogenic zone (Fig. 14d). The last 30 seconds the megathrust, between 975 kilometers and 1030 kilometers, slips simultaneously with increasing speed with time. The maximum slip rate of 6.3 m/s is reached 25 seconds before the arrest, near the downdip limit of the seismogenic zone at a depth of 58 kilometers (Fig. 14e).

The main earthquake is initiated by a change of path of the rupture into the sedimentary wedge (Fig. 16b and c). The path changes due to sediments that were brought down during the long-term phase. The rupture can't propagate on the sediment but instead reflects on it. This increases the energy in the system causing a higher slip rate and the rupture seeks the path with the lowest resistance. The elevated slip rates last for 16 seconds with a maximum value of 0.5 m/s, after which it decreases when the rupture travels downward (Fig. 16c). When the rupture propagates downward along the megathrust the slip rates increases again at a horizontal distance of 1015 kilometers and a depth of 50 kilometers (Fig. 16c). The energy in the system is locally increased due to reflections on the sediments that were brought down during the long-term phase. The updip limit of the megathrust is almost stationary during the earthquake and is at a horizontal distance of 975 kilometers (Fig. 16c). Here the boundary between the velocity strengthening sediment and the velocity weakening basalt is located. The rupture could have reached lower depths if the path followed the megathrust instead of turning into the sedimentary wedge. The downdip limit of the seismogenic zone increases with depth during the last 50 seconds (Fig. 16c) and is located in the transition area from velocity weakening to strengthening and approximately also brittle to ductile (Fig. 17a). The effective ductile viscosity on the
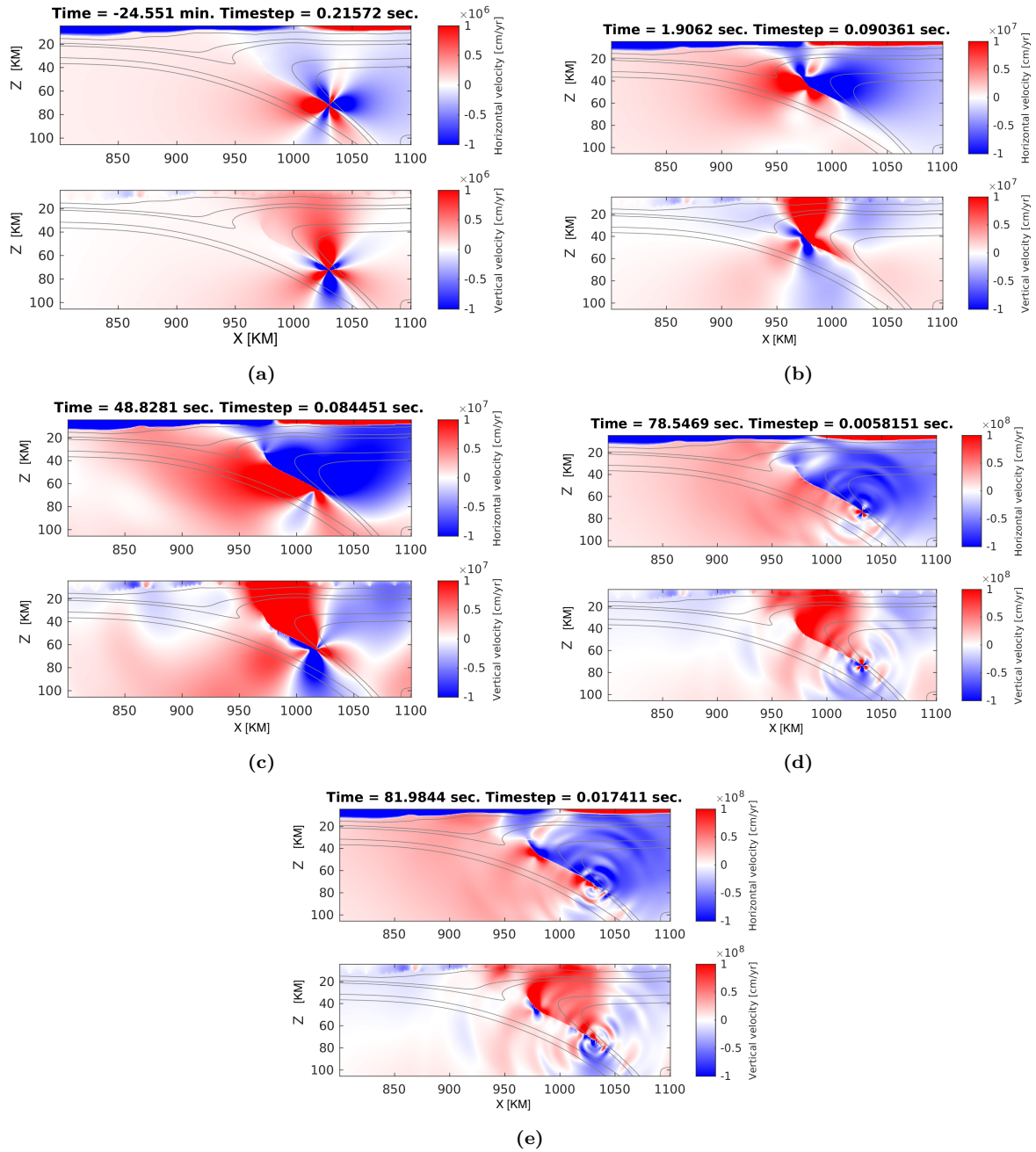
**Figure 14:** Horizontal and vertical velocity at (a) fore-shock , (b) at nucleation of main earthquake, (c) after 48.8 seconds, (d) after 78.5 seconds and (e) 81.9 seconds. Time equals zero is the moment the slip rates reach the seismic threshold at nucleation of the main shock.

fault rock decreases with depth between the 350°C and 450°C isotherm, which increases the viscous slip rate (Eq. 8). The slip rates are unpredictable in the transition zone due to large variations and heterogeneity's in impedance resulting from the local presence of sediments (Fig. 17b). The brought down sediments are still velocity strengthening with a high cohesion and slip does not form here. Eventually the rupture arrest and the postseismic phase starts. The moment of arrest is when the slip rates dive underneath the seismic threshold and do not reach higher rates any more, which is approximately after 100 seconds (Fig. 16c).
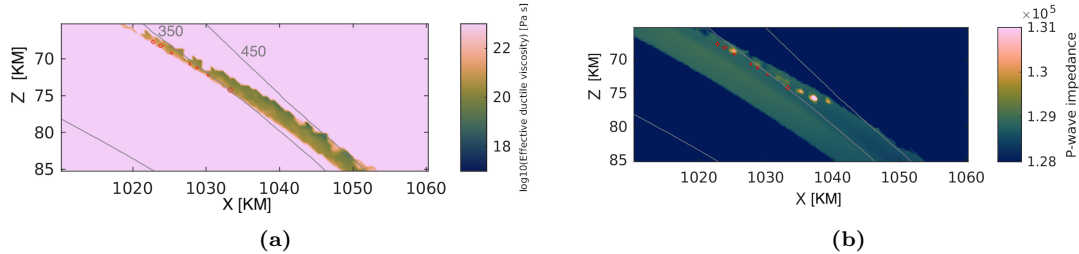


**Figure 17:** (a) The effective ductile viscosity and (b) P-wave impedance at the downdip limit of the seismic zone. Time is equal to 14e, in red the contour of a slip rate of 0.17 m/s are given and in grey the isotherms for °C.

By following the rupture coming from a horizontal distance of 975 kilometers at 70 seconds (Fig. 16b), it shows that the rupture quickly decreases in speed away from the reflection point. Eventually the propagation of the rupture is cancelled out by interference with the upward propagating rupture coming from a horizontal distance of 1025 kilometers. The amount of slip happening on the megathrust differs through time during the earthquake, but it does not decrease to zero. The rupture is continues and characterised by crack-like behaviour.
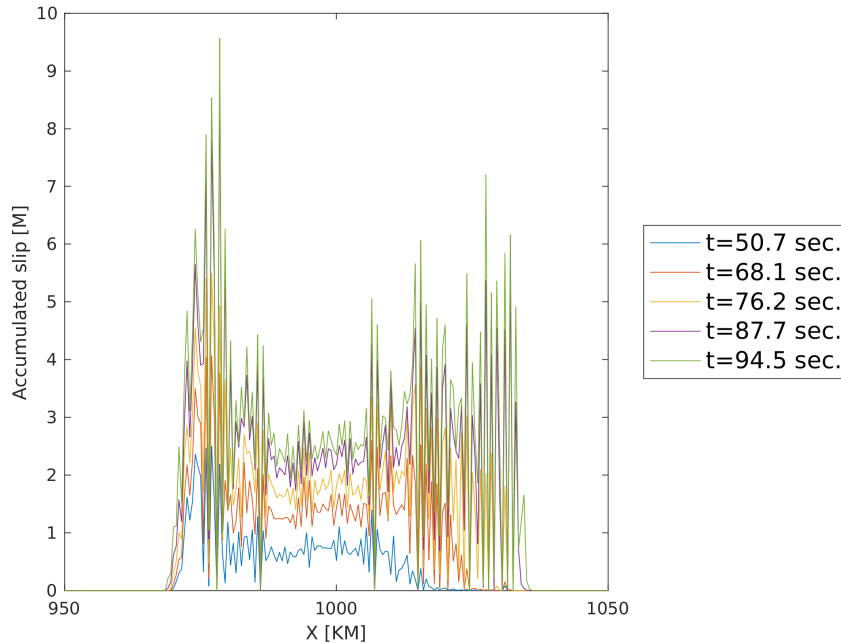


**Figure 18:** Accumulated slip for the whole earthquake at different time intervals, which are shown in the legend. The depth and horizontal distance of the points on which the accumulated slip is determined are equal to 16a.

The accumulated slip during the main earthquake is determined for different time intervals (Fig. 18). Two areas of higher accumulated slip are visible with in the middle an area where the accumulated slip is lower, only around 3 meters. At the updip limit between 970 and 985 kilometers most of the slip accumulates
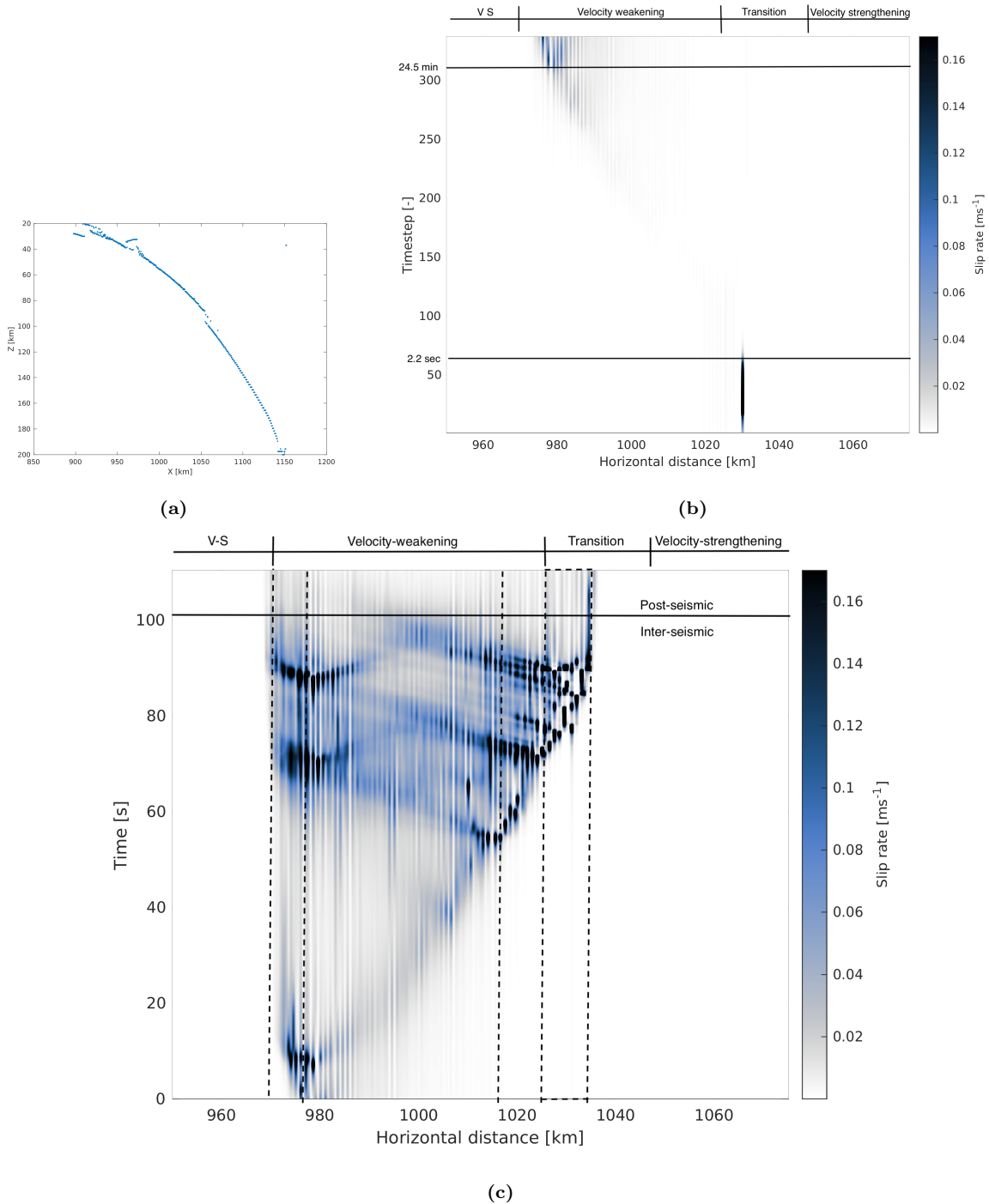
20

**(a)**



**(b)**



**(c)**

**Figure 16:** (a) The depth and horizontal distance of the nodes on which the slip rate is determined. (b) Slip rate on the megathrust during the fore-shock and propagation upwards until the start of main shock. On the y-axis time step is shown with indications of the time. (c) Slip rate on the megathrust during the main earthquake. Dotted lines are reflection surfaces. At the top the velocity weakening and strengthening zones are indicated.
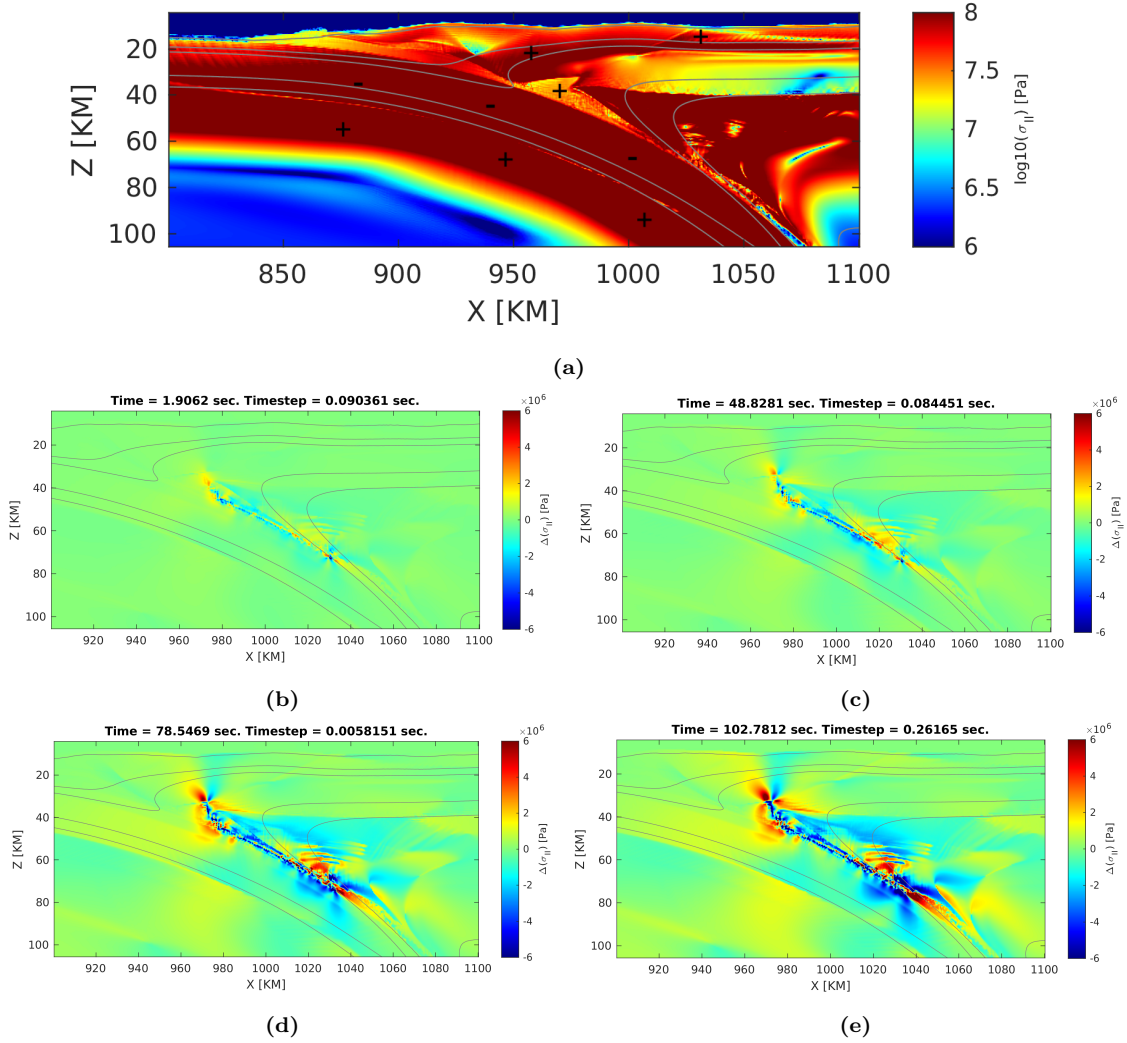
**Figure 19:** (a) Initial state of the second invariant of the deviatoric stress with + indication compression. (b) Change in second invariant of the deviatoric stress after nucleation, (c) after 48.8 seconds, (d) after 78.5 and (e) at arrest. In black the contour of a slip rate of $1 * 10^{-3}$ m/s is shown.

with almost 10 meter of slip reached at a horizontal distance of 977.5 kilometers and depth of 31 kilometers. In the dynamic rupture model of Van Zelst et al. [2019] the highest accumulated slip is also reached at the updip limit, but the slip is 5 times higher. In their model more reflections occur in the sedimentary wedge, which increased the energy in the updip limit and breaks the shallow megathrust. The downdip limit start to slip in a later stage of the event and the highest accumulated slip at the downdip limit is 7.5 meter at a horizontal distance of 1026.5 kilometers and depth of 57.8 kilometer.

The width of the slipping path is 75 kilometer and it is located completely in the seismogenic zone. The moment magnitude of a slipping patch of 75 kilometers is estimated at about 8.1, when using the empirical scaling relations of Blaser et al. [2010]

$$log_{10}W = -1.86 + 0.46M_w \tag{41}$$

### 4.1.4 Stress and Interface strength

The initial stress state of the system before the fore-shocks is as followed (Fig. 19a). There is a strong subducting oceanic slab with on top of it the faultrock with a lower second invariant of the deviatoric stress

due to a higher pore fluid pressure and lower cohesion. The faultrock has the lowest second invariant of the deviatoric stress at the surface and it increases towards the 100°C isotherm due to increasing pressure with depth. After the isotherm the stress decreases again due to the linear regression of mainly the cohesion (Fig. 9b). The lowest second invariant of the deviatoric stress is reached just below the 150°C isotherm and at the 450°C isotherm, where the brittle-ductile transition is roughly complete. The highest second invariant of the deviatoric stress in the fault rock occurs just above the 350°C isotherm, where the transition from velocity strengthening to weakening and approximately brittle to ductile slowly starts (Fig. 19a). As creep increases there, differential displacement is highest at that location, such that the stress increases fastest and therefore nucleation preferentially occurs there. The outer-band of the subducting slab is under extension due to the movement of the slab, while the inner-band is under compression (Fig. 19a). The second invariant of the deviatoric stress in the upper continental crust increases with depth throughout the wedge, while local heterogeneity's exist. The lower continental crust has a lower second invariant of deviatoric stress than the upper continental crust due to an increase of non-linear creep with temperature. The mantle underneath the continental lower crust is strong and behaves brittle until 87.5 kilometers in depth (Fig. 11b).

After nucleation the second invariant of the deviatoric stress is lowered at nucleation location and increased in front of the rupture (Fig. 19b). Between horizontal distance of 985 kilometers and 1015 kilometers a zone of increased stress is surrounded by two zones of stress drop. The lower follows the rupture path and has a higher drop in stress. The top zone is formed due to wave propagation into the mantle wedge and the increase of stress is formed due to reflections on the boundary between the fault rock and the mantle (Fig. 19b). At the 350°C isotherm the stress is lowered due to the fore-shock and at lower depths the stress is increased. Although waves have propagated into the deeper parts of the oceanic and continental mantle, there has not been a noticeable drop in stress.

After 48 seconds the rupture has propagated into the sedimentary wedge, causing a drop in the second invariant of the deviatoric stress along the rupture path (Fig. 19c). Seaward of the rupture path and at the rupture tip the stress has increased with 4 MPa. There are again two paths of stress drop visible between 985 and 1015 kilometers with the lower still following the rupture path of the downgoing rupture. The lower stress drop area has a stress drop of approximately 4 MPa (Fig. 19c).

After the arrest of the earthquake the second invariant of the deviatoric stress has decreased on average 8 MPa on the rupture path (Fig. 19e). Outside of the rupture path the stress has increased with a maximum value of 10 MPa. Here velocity strengthening material is located, which causes the stress to increase when a perturbation occurs and the rupture to come to an arrest. The faultrock located seaward of the hinge has an increase in stress of 4 MPa. The increased stress will be released as after slip in the postseismic period. Between 980 kilometers and 1020 kilometers the succession of stress drop, stress increase and again stress drop is still present (Fig. 19e). The upward movement of the continental plate along the megathrust, causes a stress increase of 7 MPa in the continental mantle around 1025 kilometers (Fig. 19e). The outer-part of the bended slab is still in extension and the inner-part is in compression due to the fast subduction of the slab during the earthquake. The outer-part has increased in stress left of the rupture, even though it encounters the same extension (Fig. 19e). This apparent difference is caused by how the second invariant of the deviatoric stress is calculated, which makes it always positive. For the inner-band there is a decrease in stress left of the rupture, while it is still under compression.

As the rupture propagates the interface strength on the megathrust decreases due to changes in the state parameter (Fig. 20a). The front of the rupture has a continues low interface strength, which is an indication of continues slip. The interface strength is more heterogeneous on the megathrust for distances further than 990 kilometers. Here the interface strength decrease temporarily when the slip rate is increased and it becomes higher again when the slip rate becomes lower. The white lines on the plot indicate locations with high interface strength on the megathrust. These are caused by the sediments, which have different friction parameters. Some of these locations are continues, while on others slip is able to form and thereby the interface strength is lowered (Fig. 20a). In general there is an increase of interface strength with horizontal distance due to increase of pressure.

The second invariant of the deviatoric stress decreases at the start of the main earthquake (purple circle in Fig. 20b). Propagation updip leads immediately to a drop in stress of 5 MPa, which increases a bit with time. At the start of the downwards propagation the drop in the second invariant of the deviatoric stress is low, around 1 MPa, which corresponds to the low slip rates at that moment (Fig. 16). With time and horizontal distance the stress drop increases to eventually a drop of 10 MPa at the downdip limit of the

seismogenic zone (Fig. 20b). The second invariant of the deviatoric stress increases away from the slipping patch for horizontal distances greater than 1035 kilometer or smaller than 975 kilometer, due to the change to velocity strengthening material. The green lines on the megathrust are at the same location as the white lines in figure 20a and are caused by the velocity strengthening sediments. If the rupture propagates into these locations the stress increases and no slip forms.
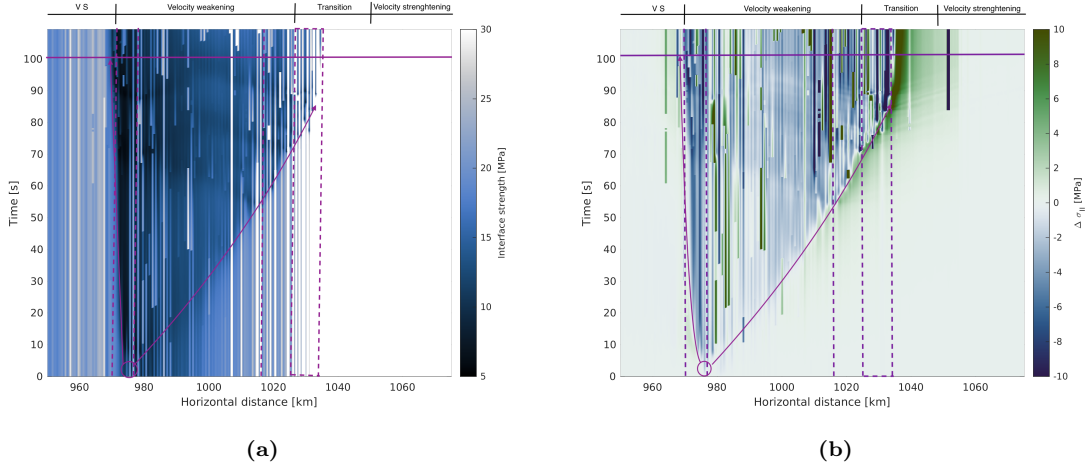


<table>
<tr><td>(a)</td><td>(b)</td></tr>
</table>

**Figure 20:** Interface strength (a) and the change in second invariant of the deviatoric stress (b) on the fault zone during the main earthquake. The purple (dotted) lines are reflection surfaces and equal to the black lines on figure 16. The change in second invariant of the stress is computed with the stress state before the fore-shock (fig. 19a).

Both the interface strength and the second invariant of the deviatoric stress decrease on the rupturing nodes and increase at the boundaries of the megathrust. At the updip limit, between the sediment basalt boundary and 980 kilometers, the drop is immediately after nucleation and continuously. While at the downdip limit the drop occurs at a later stage and increasing with horizontal distance and time. The drop in interface strength and second invariant of the deviatoric stress is very heterogeneous due to velocity strengthening sediments that were brought down into the slab.

Not only the absolute values of the interface strength and the second invariant of the deviatoric stress are important but also the difference between them. Because slip becomes noticeable in the system when the second invariant of the deviatoric stress is larger than the interface strength (Eq. 24). I have plotted the slip rate, the second invariant of the deviatoric stress, interface strength and the different between the last two to check whether this statement is correct for this simulation (Fig. 21). The time shown is 60 years and it spans the inter-, co- and very small part of the postseismic period of the main earthquake. Already in the interseismic period the second invariant of the deviatoric stress stress is higher than the interface strength, while at this moment the slip rate has a value of $10^{-9}$ m/s and is not noticeable yet (Fig. 21d). The slip rate reaches levels higher than the seismic threshold (0.17 m/s), when the second invariant of the deviatoric stress is 15 MPa higher than the interface strength (Fig. 21d). A peak in slip rate is associated with a drop in both the second invariant of the deviatoric stress and the interface strength. The drop in interface strength is larger causing a trough in the difference between them (21d).

The red line does not have any spikes in the slip rate and has much lower slip rate, even though the difference between the interface strength and the second invariant of the deviatoric stress is larger than for the blue line. Both the interface strength and the stress are decreasing smoothly for the red line instead of with many peaks and troughs, which causes the slip rate to be stable around 0.15 m/s. After 4000 time steps the slip rate is lowered beneath the seismic threshold and the rupture comes to arrest. The interface strength is increased causing the difference with the second invariant of the stress to be less than 15 MPa.

From these observations I can conclude that for high slip rates the drop in the second invariant of the stress and the interface strength are instant instead of smooth and that the absolute value between them does not matter. Next to that the slip rate reaches the seismic threshold if the difference between the second invariant of the deviatoric stress and the interface strength is larger than 15 MPa. Herrendörfer et al. [2018] has defined the interface strength as the moment slip becomes noticeable but never what the exact value of

the slip is at this moment. So it possible that this deviation is caused by a difference in definition of when slip is noticeable. Another possibility is that the cohesion has an effect on the interface strength, which is not taken into account by the calculation (Eq. 24).
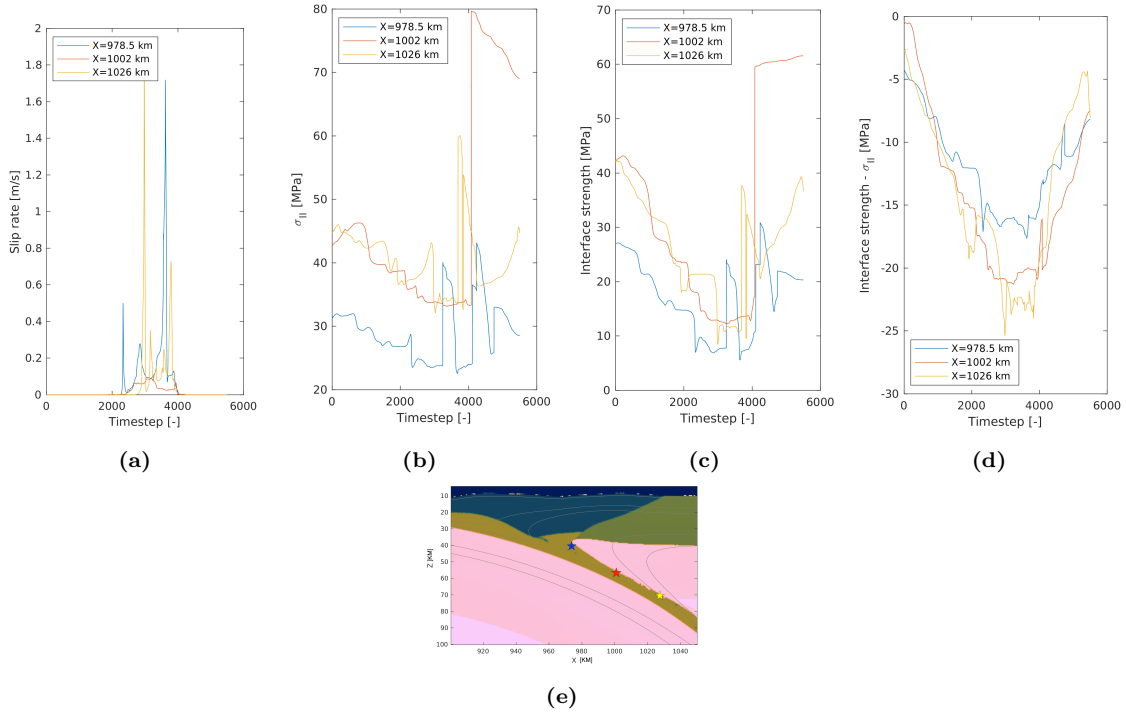


**Figure 21:** (a) Slip rate, (b) second invariant of the deviatoric stress, (c) the interface strength and (d) the difference between the last two or almost 6000 time steps. (e) Location of the three nodes overlain by the isotherms and shear wave impedance. The first node, blue line, is located at the first peak of the accumulated slip (Fig. 18). The third node, yellow line, is located at the second peak of the accumulated slip and the second node, red line, is in the middle of the two peaks.
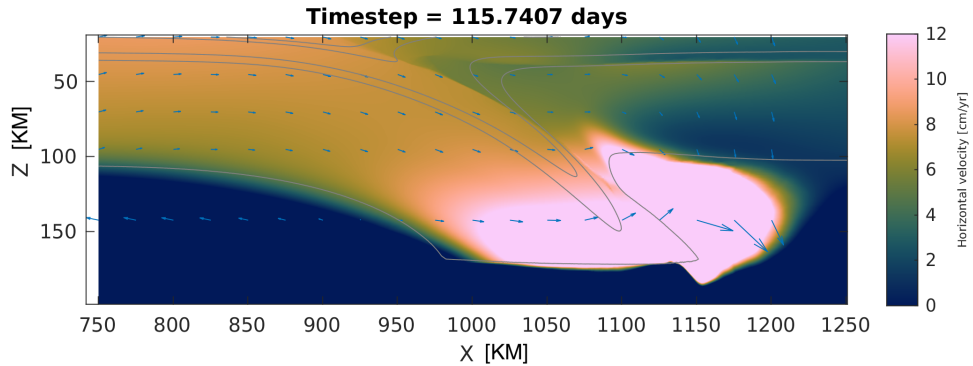
## 4.2 Slow slip events



**Figure 22:** Velocity arrows plotted over the horizontal velocity in interseismic velocities of the simulations with 22 slow slip events before one earthquake nucleates.

Slow slip events can occur as events before an earthquake or in models that do not contain any seismic events. To analyze the slow slip events, I have decided to look into a model, that contains 22 slow slip events

25

before an earthquake occurs with a maximum slip rate of 2.5 m/s and duration of 10 seconds (24b). The values of the friction parameters of this simulations are 0.019 for the direct effect, 0.011 for the evolution effect and the characteristic slip distance is 0.1 meter. Already in the interseismic period a change is visible compared to the simulation of the reference earthquake (Fig. 10b and 22). The time step is 115 days instead of 72 days, the velocity in the slab is close to the push velocity and downwards except for at the end, where the velocity quickly increases to 18 cm/yr. The movement of the subducting plate is partly passed on to the continental plate, which moves landward with a speed of 6 cm/yr. The downward movement of the continental plate from 1125 kilometer is still present, even though the upward push of the mantle underneath the mantle has become smaller.

The slow slip events in the simulation are periodical between 1000 and 2000 years with a recurrence interval of 125 years. At the start and end of the simulation the recurrence interval is a bit disturbed due to larger events, after which a longer time is needed for the next event to occur. The events with larger slip rates show an increase in amount of time step, while the duration of the time step becomes shorter. The maximum slip rate of the larger events is $10^{-5}$ m/s and can last for days, while the maximum slip rate of the smaller events is $10^{-8}$ m/s and can last for months (Fig. 24b). Events with a smaller maximum slip rate have less yielding nodes than events with higher slip rates (Fig. 24 and 23). The events with a maximum slip rate of $10^{-8}$ m/s are located between the downdip limit of the seismic zone and horizontal distance of 940 kilometers, while the faster events pass this and slip the whole megathrust. To identify the characteristics of the slow slip events we will look at two events, which are circumscribed in figure 24b.
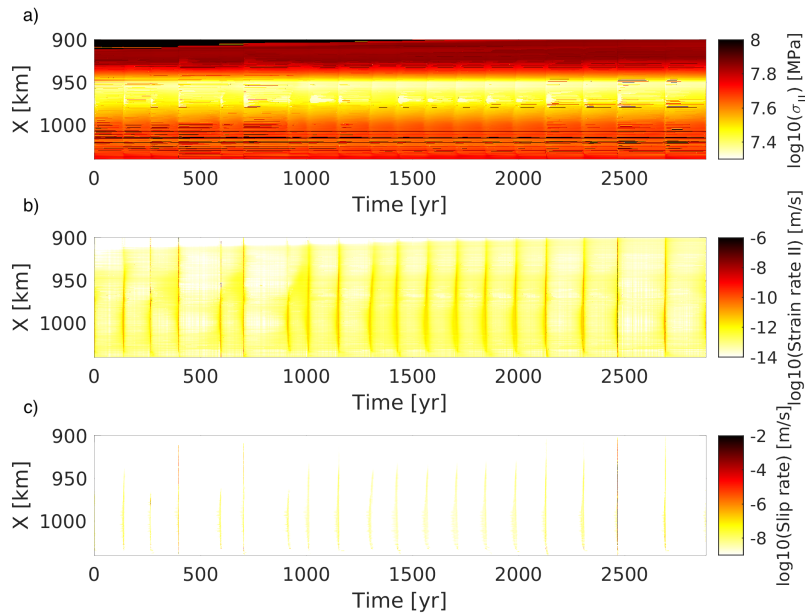


**Figure 23:** Second invariant of the deviatoric stress (a), strain rate (b) and slip rate (c) for nodes on the megathrust through time.

The first event has a maximum slip rate of $3.38 * 10^{-9}$ m/s, a minimum time step of 34 days and a duration of 20 years, which is resolved in 182 time steps. The slow slip event starts at the downdip limit of the seismogenic zone and causes the continental plate to move seaward and up with a speed of approximately 4 cm/yr (Fig. 25a). The velocity is highest at the downdip limit and decreases upward. The oceanic plate has almost no horizontal movement and moves up until a horizontal distance of 925 kilometers (Fig. 25a). During the event the slip rate increases in the continental plate to 8 cm/yr (Fig. 25b). The subducting plate starts to move seaward with an speed of 4 cm/yr due to the push of the mantle of the continental plate. The slab does not subduct into the mantle anymore and has an upward movement instead (Fig. 25b). The effect of the continental plate on the subducting plate decreases when the rupture propagates upward (Fig. 25c). At this moment the highest velocity of 9cm/yr is reached around 975 kilometer. At the end of the event the

velocity of the continental plate decreases to 4 cm/yr and the subducting plate moves landward again (Fig. 25d). Both the continental and subducting plate still move upwards, except for the slab for a horizontal distance further than 975 kilometers. The viscosity of the megathrust is homogeneously lowered to $10^{19}$ Pa·s (Fig 25e). There are no patches of higher viscosity present that resist the slip, which are found in nature for slow SSE's. Beyond the down an updip limit of the seismogenic zone the viscosity is higher because no slip has taken place there.
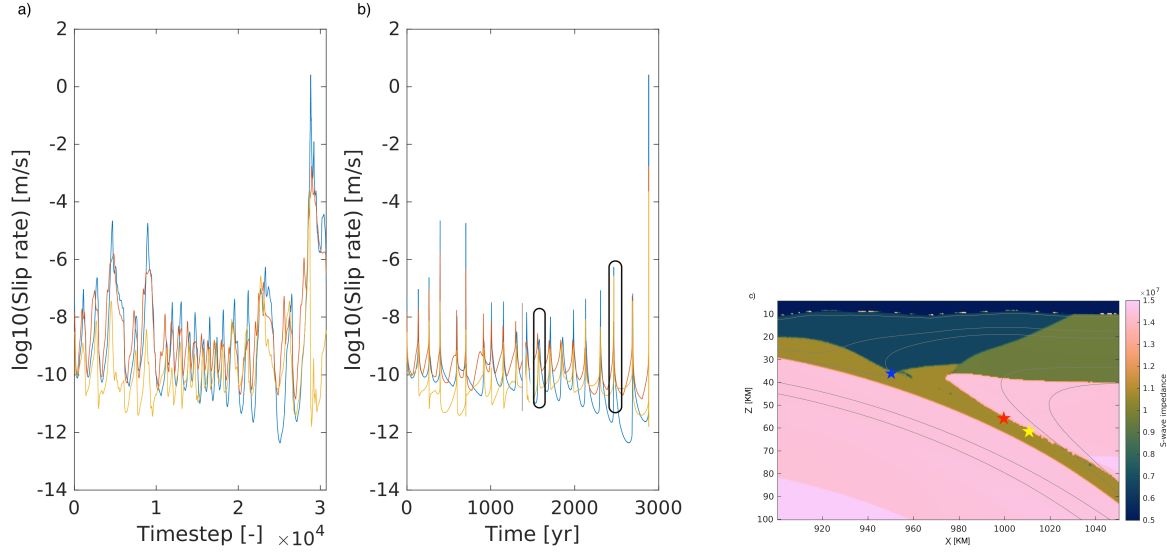


**Figure 24:** Slip rate per time step (a) and slip rate per time on three nodes in the seismic zone. Time equals zero after transition to RSF. (c) Location of the three nodes with the S-wave impedance and the isotherms in grey.

The second event has a maximum slip rate of $1.8 * 10^{-5}$ m/s, a minimum time step of 9 minutes and a duration of 29 days, which is resolved in 1276 time steps. The velocities before the event are similar to the velocities of the first slow slip event. The continental plate is moving seaward and up, pushing the subducting plate seaward (Fig. 27a). Almost the whole subducting plate moves up and seawards except for at the fault zone between 975 and 1025 kilometers (Fig. 27a). The velocity of the subducting plate changes to landward just before the event, except for the deeper parts of the slab (Fig. 27b). The subducting plate moves upward until 960 kilometer, where it switches to downward. Most of the slip occurs an the top part of the seismogenic zone (Fig. 27b). During the event the whole subducting plate moves landward with increasing speed towards the fault, where it reaches a velocity higher than 2000 cm/yr (Fig. 27c). The subducting plate moves upward except for below the downdip limit of the fault. Slip occurs on the whole width of the seismogenic zone, the slip follows the path of the faultrock and does not move into the sedimentary wedge as happens in the earthquake of the reference model (Fig. 27c). The continental plate moves up and seaward with a maximum velocity higher than 2000 cm/yr. During the event both the continental and subducting plate increase in speed and the slipping patch increases into the transition zones (Fig. 27d). After the event the highest slip rates, approximately 300 cm/yr, are reached in the transition and velocity strengthening zones of the faultrock, where the stress has increased during the event (Fig. 27e). At the updip limit the slip almost reaches the surface, while at the downdip limit the slip does not propagate beyond the 350°C isotherm, due to the brittle-ductile transition. The movement of the subducting plate is still landward but has decreased a lot in speed and the movement is changing up and down from 950 kilometers onward (Fig. 27e). The movement of the plates is very similar to the postseismic movement of the main earthquake of the reference simulation (Fig. 26). Only the speed of continental plate near the mega thrust is much higher, 1000 cm/yr instead of 300 cm/yr, for the main earthquake and the slip does not reach the surface due to change in path. The viscosity on the fault rock including the velocity strengthening material above the updip limit has decreases homogeneously to $10^{17}$ Pa·s (Fig. 27f).
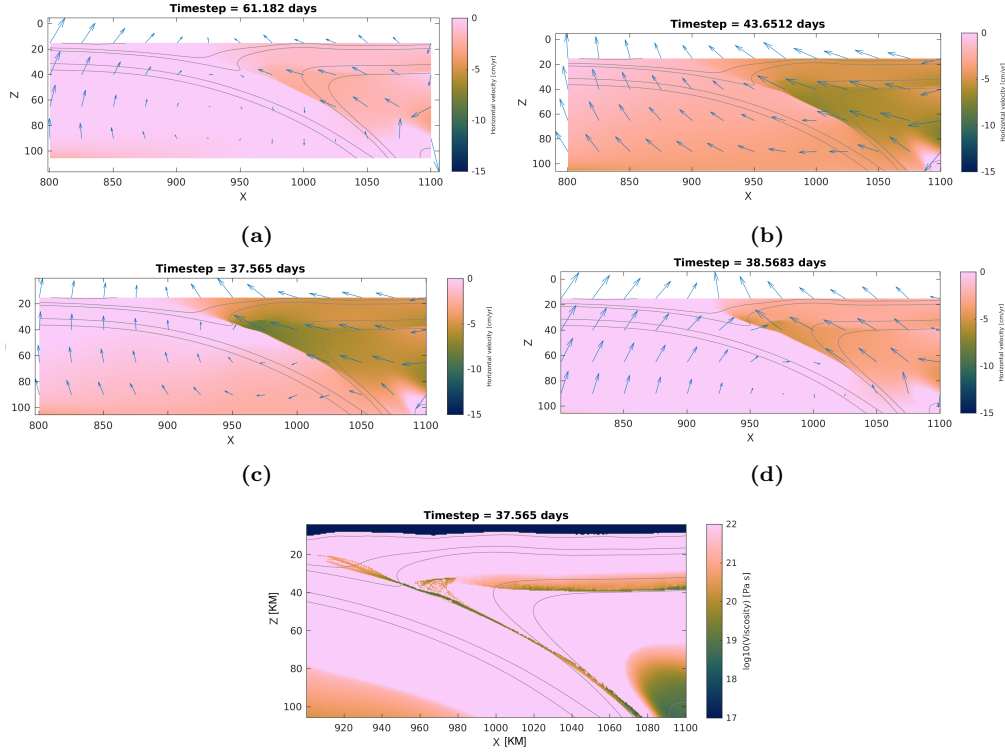
**Figure 25:** (a-d) Velocity arrows plotted over the horizontal velocity for different phases of a slow slip event in the first class. The subplots are in chronological order. (e) Viscosity during the event.
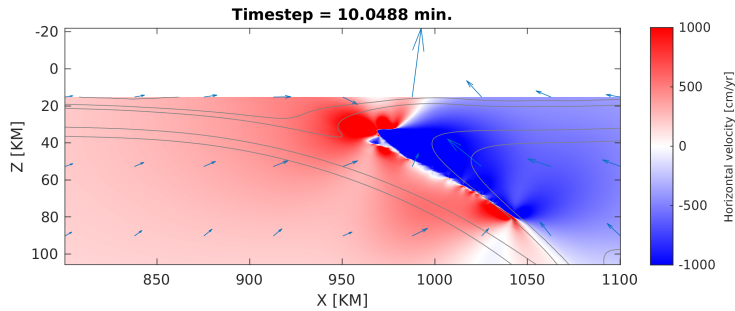


**Figure 26:** Velocity arrows plotted over the horizontal velocity in the post-seismic period after the reference earthquake.

From these two examples we can conclude that the slow slip events with the higher maximum slip rates behave more like fast earthquakes. Except that there are no waves visible and there is less downward movement of the slab. The behaviour of the slower slow slip events are a lot different and are dominated by the movement of the continental plate that pushes the subducting plate towards the sea. The viscosity on the megathrust decreases to values under $10^{17}$ Pa·s for the fast slow slip events, while viscosity is $10^{19}$ Pa·s for the slow slip events. The slow slip events occurring before the reference earthquake have the same behaviour as the slower slow slip events.

## 4.3   Behaviour of the model

I conducted a parameter study to identify the regimes delineating seismic slip, aseismic slip and constant creep in the model. The behaviour of a model is mainly defined by the ratio between the width of the velocity
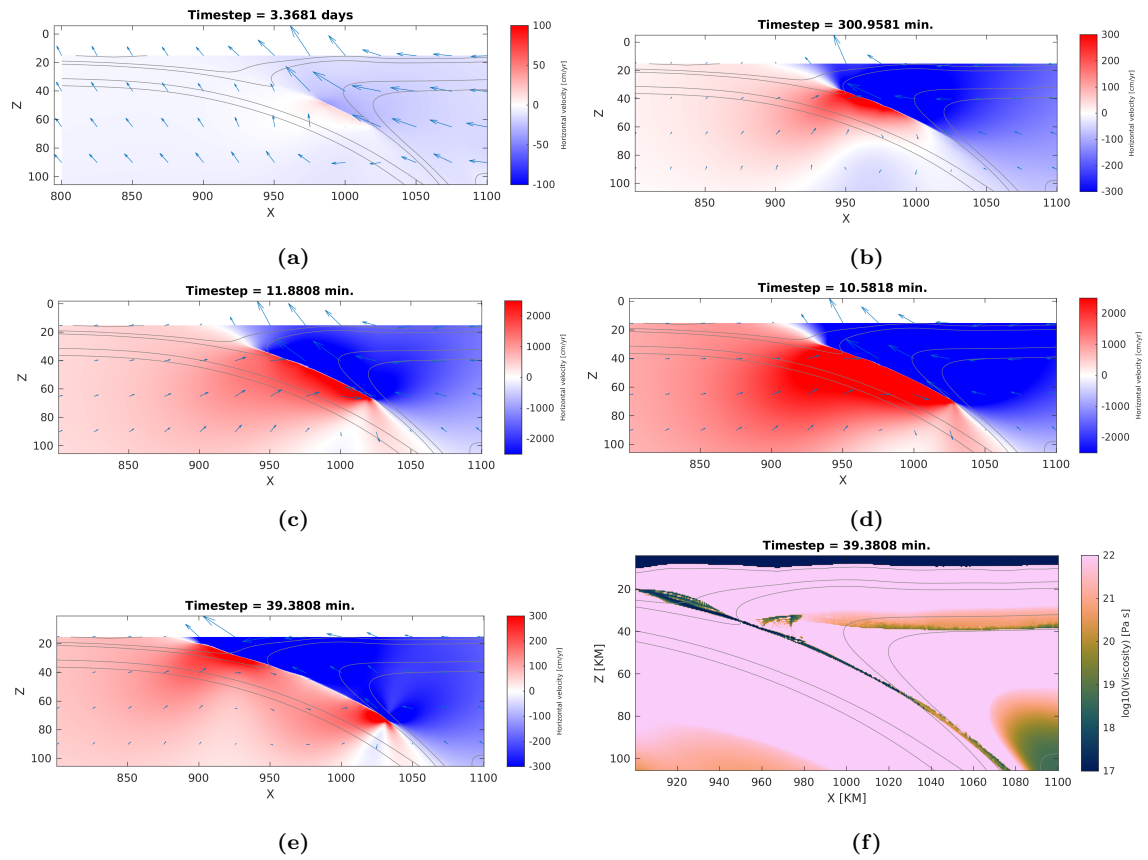
**Figure 27:** (a-e) Velocities arrows plotted over the horizontal velocity for different phases of a slow slip event in the second class. The subplots are in chronological order. (f) Viscosity during the event
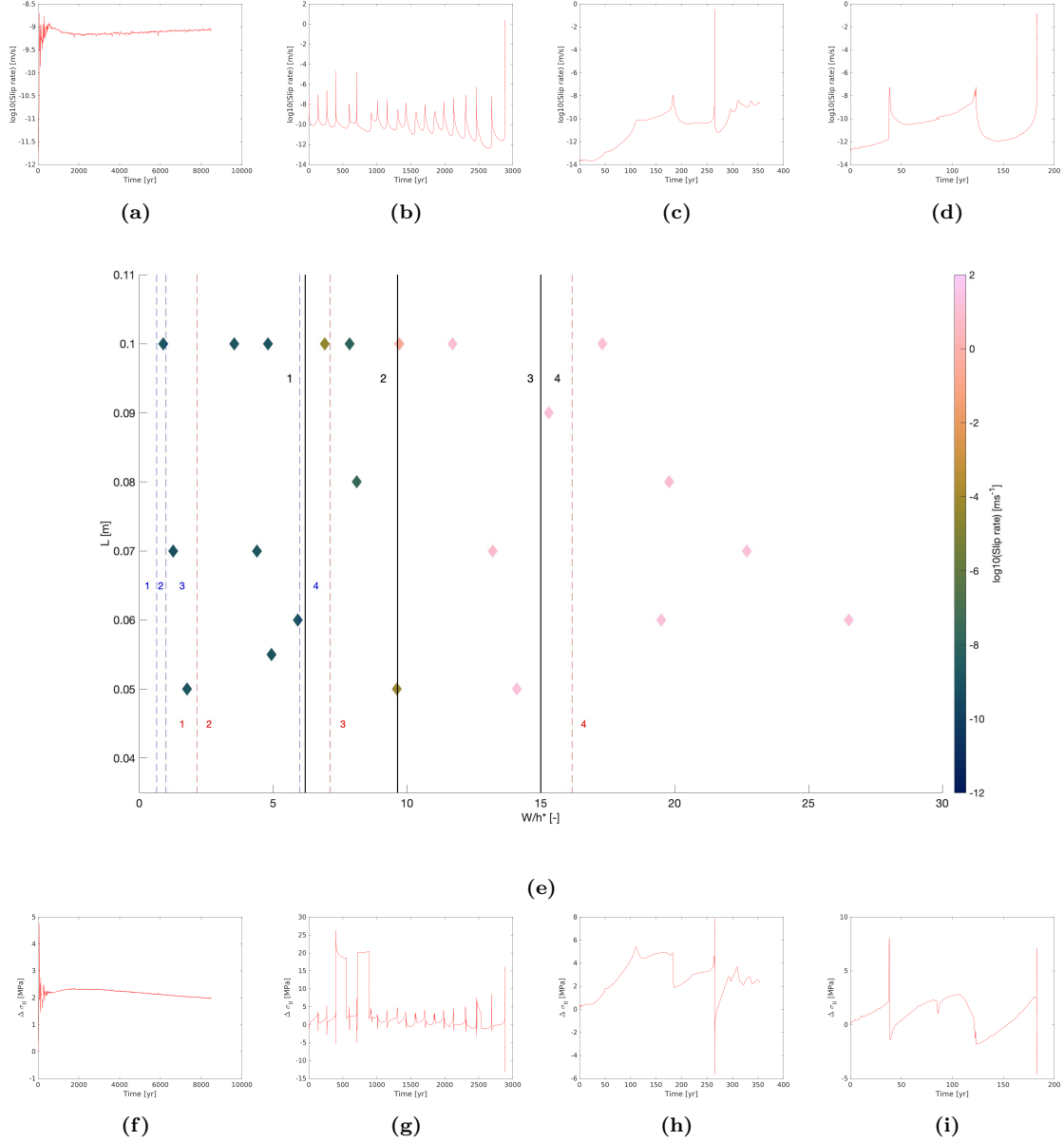
**(a)** **(b)** **(c)** **(d)**



**(e)**



**(f)** **(g)** **(h)** **(i)**

**Figure 28:** e) Slip spectrum expressed as slip velocity, as a function of $W/h^*$ and L. The solid black lines are the boundaries of our modelled behaviour, the blue dotted lines are the boundaries of Herrendörfer et al. [2018] and the red dotted of Liu and Rice [2007]. Panels a-d show the slip velocity in the simulations and panels f-i show the second invariant of the deviatoric stress. Four different regimes are identified in the STM-RSF model: (a and f) Stable sliding with small decaying oscillations. (b and g) Periodic slow slip events. (c and h) Multiple slow slip events and one earthquake. (d and i) Multiple slow slip events and one earthquake with a higher slip rate.

weakening zone (W) and the nucleation size $h^*$ [Liu and Rice, 2007; Herrendörfer et al., 2018] defined as,

$$h^* = \frac{2}{\pi} \frac{GbL}{(b-a)^2 P(1-\upsilon)})$$ (42)

which is dependent on the values of the direct effect (a), the evolution effect (b), the characteristic slip distance (L), the pressure (P), the poisson ratio ($\upsilon$) and the plastic potential fraction (G).

The 22 models that are run can be divided into four different regimes (Fig. 28). The first regime is for $W/h^*$ values smaller than 6.2, this regime is characterised by stable sliding with small decaying oscillations after the initial loading phase. During the initial loading phase the model finds a new balance, the slip rate increases with almost three orders of magnitude to $1.5 * 10^{-9}$ m/s, which is close to the loading rate Fig. 28a). The second invariant of the stress increases with 2 MPa (Fig. 28f).

The second regime has a $W/h^*$ value between 6.2 and 9.65 and is characterised by periodic slow slip events, which decay towards stable sliding or increase towards one seismic slip event and afterwards stable sliding. The last possibility is shown in figure 28b and g, most events do not reach a slip rate higher than $10^{-6}$ m/s and have a stress drop around 5 MPa. The time step is variable between days and months due to the fluctuations in slip rate. A more detailed description of the slow slip events has been described in the previous section 4.2.

The third regime has a $W/h^*$ value between 9.65 and 15, this regime is characterised by earthquakes, although some slow slip events may proceed it. The earthquake has a maximum slip rate of around 8 m/s (Fig 28c). After the earthquake oscillations occur after which the behaviour changes to stable sliding. The second invariant of the deviatoric stress increases after the transition to RSF and drops with almost 14 MPa during the earthquake (Fig 28h). The second invariant of the deviatoric stress is 2 MPa higher during stable sliding than before the transition and the slip rate has increased by almost 4 magnitudes to $10^{-9}$ m/s. The values of stable sliding after the earthquake are equal to the values of regime 1 and to the push velocity.

The last regime has a $W/h^*$ value higher than 15, this regime is characterised by slow slip events and one earthquake with a maximum slip rate around 15 m/s. These models stop due to problems caused by fast up welling of mantle material at the right lower boundary (Fig. 13). The first slow slip event is accompanied by a large drop in stress and fast increase in slip rate (Fig. 28d and i). Although the maximum slip rate of the second slow slip events is close to the first event the stress drop is much lower and flatter. The stress drop at the earthquake is around 10 MPa which is lower than for the earthquake in regime 3 but this earthquake is not finished yet so the stress drop can still increase.

Even though regime 3 and 4 have the same characteristics right now, I decided to separate them into two different regimes. For both regimes the problems with the lower boundary condition have an effect on the continuation after the first earthquake and I think that more earthquakes would occur if the problems are solved. Comparing the different regimes to the regimes of Herrendörfer et al. [2018] I expect that regime 3 will be periodic events, while regime 4 will be aperiodic. This is a very large assumption and it is possible that this division will change.

# 5 Discussion

I have separated the discussion chapter into five different parts. In the first four the results of my model are compared to previous studies and in the last part the limitations and future work are discussed.

## 5.1 Seismic cycle model of Van Dinther et al. [2013b].

As explained in the introduction the RSF-STM code is an adaptation of the geodynamic seismic cycle (STM) model of [Van Dinther et al., 2013b]. By applying the changes discussed in section 2 the velocities in the coseismic period are increased by 4 orders of magnitude, from $2.8 * 10^{-5}$ m/s to 0.17 m/s, in the STM-RSF model and the duration is decreased from 97 years to minutes. Moreover, in the STM-RSF model waves are formed and they propagate through the model. In the STM model the megathrust slips until near the surface, which does not happen in the main earthquake of the reference simulation due to the path change beneath the sedimentary wedge. The slow slip events of the second class in the simulations in regime 2 continue until the surface. During these events there is no formation of waves and these events resemble the earthquakes of the STM model more (Fig. 27d).
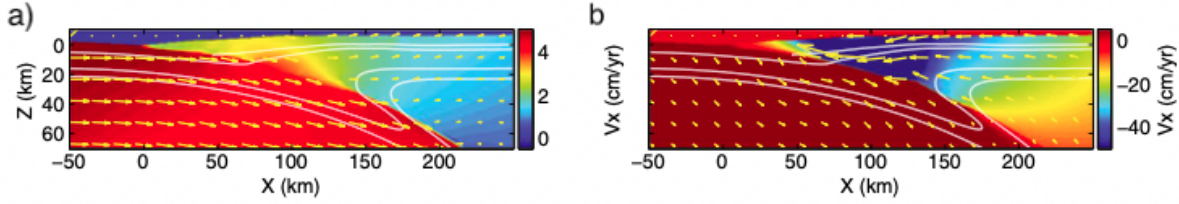
**Figure 29:** Horizontal velocities of seismic cycle model of [Van Dinther et al., 2013b] with (a) one time step before and (b) at the peak of an event.

There are some differences in the interseismic period between the STM model and the STM-RSF model. First of all the horizontal velocity is much higher in my model than in the STM model, 18 cm/yr compared to 4 cm/yr, even though the push velocity is the same (Fig. 29a and 10b). The velocity in the crust of the continental plate in the STM-RSF model first decreases away from the plate interface to increase again around 1025 kilometer (Fig. 10b). For the STM model the pattern is turned around, the velocity first increases away from the plate interface and switches to decreasing at 110 kilometers from the trench (Fig. 29a). The difference in speed at the trench is caused by the higher cohesion in the STM-RSF models at the top of the fault rock, which causes coupling between the continental and subducting plate. The other changes in horizontal velocity are caused by the downward movement of the continental crust and mantle from 1150 kilometer and by material flowing up below the slab.
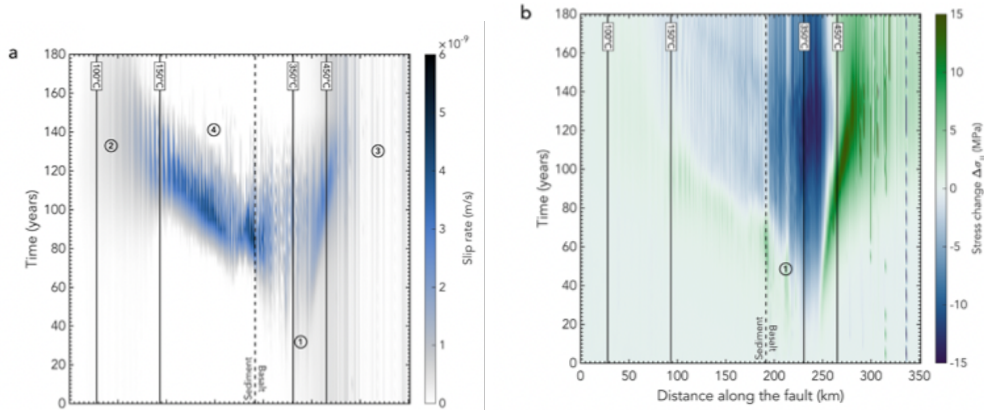


**Figure 30:** (a) Slip rate evolution with time and (b) temporal stress change evolution for the STM model of [Van Dinther et al., 2013b], adapted from [Van Zelst et al., 2019].

Van Zelst et al. [2019] used the same seismic cycle model to link one event to the dynamic rupture model, but they also examined the space-time evolution of the original event in the STM model (Fig. 30). A comparison of figure 30a with figure 16, shows again that the slip rate in the STM-RSF model is 8 order of magnitude higher. There are multiple rupture paths visible in my model due to reflections, while in the STM-model there are only two rupture fronts propagating. One upwards from nucleation and one downwards without any reflections.

The pattern of change in the second invariant of the deviatoric stress of the STM model (Fig. 30b) and of my STM-RSF model (Fig. 20b) reveal some differences. The STM-RSF model contains two areas of large decrease in stress with the highest stress drop between the hinge and the updip limit of the seismic zone and the second area located around the 350°C isotherm. Between the areas of high stress drop the change in stress is very heterogeneous with variations in both space and time. The STM model contains one area of high stress drop around the 350°C isotherm with a homogeneous and smooth decreasing amount of stress drop upward. The largest change in second invariant of deviatoric stress is 15 MPa, which is 5 MPa higher than the largest stress drop in the STM-RSF model. Both models have an increase in stress downdip of the fault. The difference in pattern is caused by the reflection of waves in the STM-RSF model which (re-) activates

different parts of the megathrust during the event and the presence of velocity strengthening sediments with a very high cohesion on the megathrust.

## 5.2  Coupled dynamic model of Van Zelst et al. [2019].

In the dynamic rupture model of Van Zelst et al. [2019] the rupture is predominantly crack-like, although pulse-like behavior is observed in the sediments. The maximum slip rate in the DR model is 10.9 m/s, which is reached as the rupture tip reaches the sediment-basalt transition. The maximum slip rate in the STM-RSF is 4 m/s slower and is reached near the downdip limit of the seismogenic zone. The duration of the earthquake is similar both being around 100 seconds.
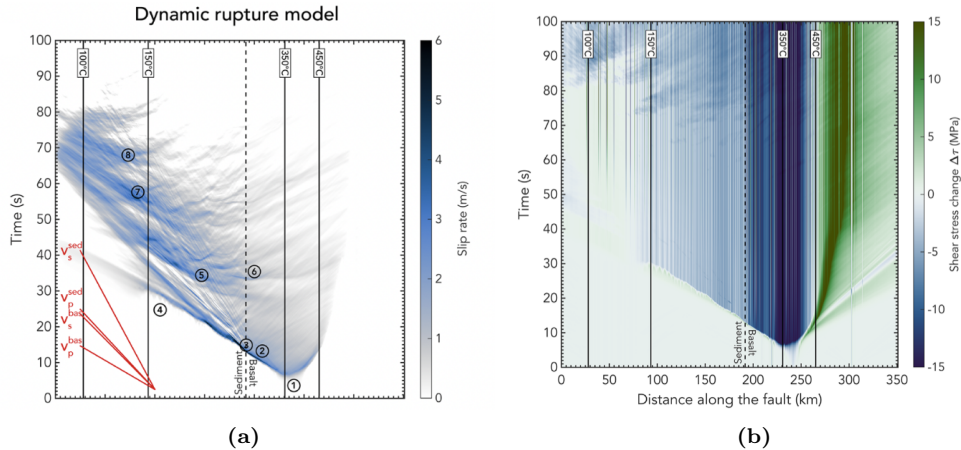


**Figure 31:** (a) Slip rate evolution and (b) stress change of the earthquake in the coupled dynamic model of Van Zelst et al. [2019].

After nucleation the rupture propagates mainly upwards along the megathrust in the DR model, where it reflects on the sediment-basalt boundary causing re-activation of the fault [Van Zelst et al., 2019]. The rupture comes to a spontaneous arrest below the limit of the seismogenic zone, while the shallow megathrust breaks due to surface reflections providing additional energy. 50 seconds after the earthquake the waves are trapped in the accretionary wedge, causing continuous fault reactivation and increasing the slip of the shallow part of the fault. The largest difference between the DR model and the STM-RSF model is the accumulated slip at the updip limit of the seismogenic zone, which is almost 5 times higher for the DR model. In the DR model the maximum accumulated slip is 57.9 meter in the sediments, while in the STM-RSF model it is 10 meter in the basalt near the updip limit. This difference is partly numerical and partly due to differences in lithological structure. In my STM-RSF model there are no incoming sediments, which causes the sediment-basalt boundary to occur almost 100 kilometer less deep. By adding the incoming sediments on the accretionary wedge to a homogeneous medium with a reflecting surface a low-velocity region is introduced (Fig. 32c) [Van Zelst et al., 2019]. This increases the portion of trapped seismic waves in the sediments, which results in a complex slip reactivation pattern on the fault. The rupture behaviour changes from crack-like to pulse-like and the accumulated slip on the fault is increased in the sediments [Van Zelst et al., 2019]. The sediments that are brought down during the long-term phase in the STM-RSF model do cause some reflections but the amount of sediments are very sparse compared to the DR model. Not only the amount of sediment is increased in the DR model but they also have different friction parameters. The sediments in the DR model are temperature dependent velocity weakening which makes it possible for the rupture to propagate into the sedimentary wedge. In the STM-RSF model the sediments are velocity strengthening with a very high cohesion, causing the rupture to arrest when hitting the sedimentary wedge.
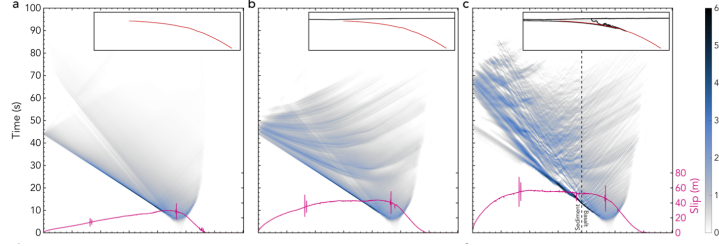
**Figure 32:** Slip rate evolution of a megathrust earthquake rupture for (a) a homogeneous model, (b) a homogeneous model with a free surface top boundary condition, (c) the model of (b) with incoming sediments added. All figures are adapted from Van Zelst et al. [2019].

The slip rate, fault slip and rupture duration should increase when an free surface is added due to reflection of the waves (Fig. 32b) [Van Zelst et al., 2019]. Even though my model contains a reflecting surface, there seems to be no (re-) activation of the fault due to the waves reflecting from the surface. The waves either die out when reaching the surface or on their way back before reaching the megathrust interface (Fig. 33). This is caused by the lower rupture speed in the STM-RSF model than in the DR model. The rupture propagates with a speed of 1750 m/s in the sediment in the DR model, while the rupture speed is only 625 m/s in the STM-RSF model.

In the dynamic rupture model the fault is predefined and the shear stress is used to determine whether plastic deformation occurs instead of the second invariant of the deviatoric stress (Eq. 18). To couple the dynamic rupture model with the seismic cycle model the stresses needed to be converted by abstracting the pressure component of the deviatoric stress [Van Zelst et al., 2019]. This conversion is not needed to compare the change in shear stress during the event in the DR model with the change in the second invariant of the deviatoric stress in the STM-RSF model, because the pressure is constant during the coseismic period. The stress change in the DR model is homogeneous and smooth just like the STM model. The largest stress drop of 14 MPa occurs near the 350°C isotherm and the magnitude of the drop becomes smaller upward. From 450°C the shear stress increases, due to slip not reaching this area. The change in shear stress is higher in the DR model than in the STM model and it propagates faster away from the nucleation area. Even though sediments are present in the DR model the stress change is still homogeneous, because the sediments have a velocity weakening behaviour instead of strengthening and a low cohesion, which causes the sediments to slip. The main differences in the stress change are caused by the difference in nucleation depth, the amount of reflections and the different friction parameters of the sediment.
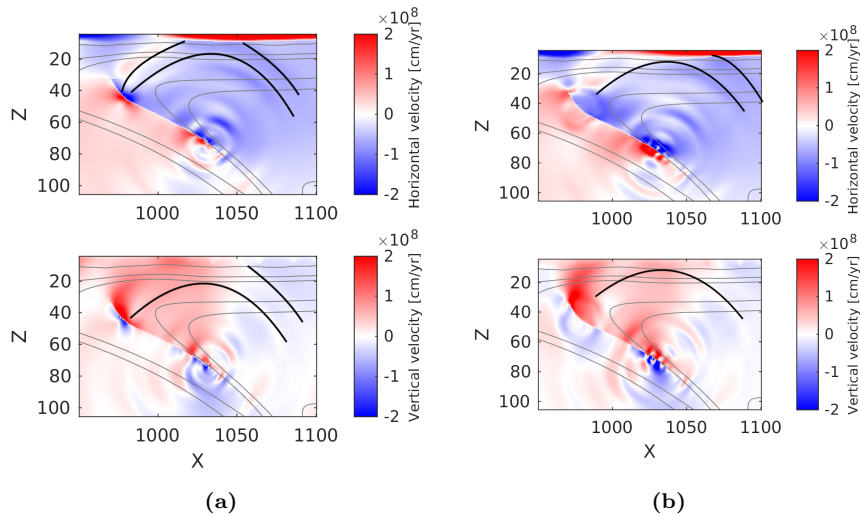


**Figure 33:** Horizontal (top) and vertical velocity (bottom) with in black indicating a wave front. Subplots (a) is 2.5 seconds before subplot (b).

## 5.3 Model behaviour comparison

Herrendörfer et al. [2018] has done a similar parameter study for the rate- and state-dependent friction code to determine the behaviour in a strike-slip setting. They also classified four regimes, which are shown by the blue dotted lines in figure 28e. Their first regime is until a value $W/h^*$ of 0.65 and consist out of decaying osculations towards stable stabling with a speed equal to the tectonic loading rate. The behaviour of their first regime is equal to the behaviour of the first regime in the STM-RSF model, only the switch to the second regime takes place for an almost 10 times higher $W/h^*$ value in the STM-RSF model. Their second regime is periodic aseismic slip events after an initial loading and stabilizing period. The slow slip events in this regime all have the size, speed and this behaviour occurs for $W/h^*$ values between 0.65 and 1. The behaviour in the second regime is comparable to the behaviour in our second regime, except that the slow slip events can differ in size from each other and that it occurs for $W/h^*$ values between 6.2 and 9.65. The third and fourth regime of Herrendörfer et al. [2018] are periodic seismic slip and aperiodic seismic slip with increasing slip rate for larger characteristic slip distance. From the third regime our model also contains seismic events, but due to the problems with the lower boundary it is not possible to divide the behaviour into periodic and aperiodic. Overall the behaviour of STM-RSF model of the subduction zone setting is similar to the behaviour of the RSF-model of the strike-slip setting. Both have four regimes with earthquakes forming from the third regime onwards. A large difference between the two is that in the strike-slip setup a large event forms in the stabilizing period of all four regimes, which does not occur in the STM-RSF model. The $W/h^*$ values for the different regimes are increased by a lot, which is caused by the change to a subduction zone setting.

This suggestion is partially supported by Liu and Rice [2007], who have conducted conducted a comparable parameter study for their 2D numerical subduction fault model with rate- and state-dependent friction. They also classified the behaviour of their model into four regimes, which are shown by the red dotted lines in figure 28c. Their first regime consisted of oscillations that decay to stable sliding with a slip rate of $2*10^{-10}$ m/s. The regime occurs until $W/h^*$ ratio of 2.16 and is comparable to the first regime of the STM-RSF model, except that the speed of stable sliding is a magnitude smaller than ours. Simple periodic oscillations occur in their second regime, these oscillations are aseismic and fluctuate between slip rates of $10.5*10^{-11}$ m/s and $6.5*10^{-11}$ m/s. The third regime consist out of complex periodic or aperiodic oscillations with slip rates between $1.6*10^{-9}$ m/s and $0.2*10^{-9}$ m/s. The behaviour in the second regime is comparable to the behaviour of the second of third regime of Liu and Rice [2007]. Both contain aseismic slip events, but the events in the STM-RSF have a maximum slip rate that is 4 magnitudes larger. If more simulations are run in the STM-RSF mode it could be possible to deviate the two different regimes. Seismic events form in the fourth regime of Liu and Rice [2007] for $W/h^*$ values larger than 16.17, the events can differ per size and are alternated with slow slip events. This regime is comparable to regime three and four in the STM-RSF model. The transition to seismic events take place for higher $W/h^*$ values in the model of [Liu and Rice, 2007], which can be caused by differences in model setup and complexity, including driving velocities and heterogeneity's.

## 5.4 Slow slip event

Episodic slow slip events and associated tremor signals are most commonly associated to occur within a temperature range of about 400-550°C [Behr and Bürgmann, 2021]. This zone is called the "ETS zone" and is located down dip of the seismogenic zone, it is fluid-rich and very overpressured due to metamorphic dehydration reactions in the subducting oceanic crust [Behr and Bürgmann, 2021]. In the ETS zone the brittle to ductile transitions also occurs. On the other hand studies suggest that in subduction zone settings the slow slip events are not restricted to specific temperature regimes or depth [Saffer and Wallace, 2015]. Shallow slow slip events have been recorded in multiple subduction zone areas and with different characteristics. At New Zealand's Hikurangi margin the SSEs have a magnitude of 6.0-7.0, recur every 1-2 years, are at a depth of 5-15 kilometer and cover a broad range of temperature (85-230°C) [Saffer and Wallace, 2015]. While the SSEs at the Costa Rican margin are much shallower within a temperature range of 12-60°C [Saffer and Wallace, 2015]. The common factors of these SSEs is that they occur along the most severely overpressured locations of the plate interface where the pore fluid ratio, $\lambda$, range from 0.4 to $> 0.9$ and in heterogeneous fault zones with different types of slip behaviour [Saffer and Wallace, 2015].

In our models the slow slip events all form in the seismogenic zone and not in the ETS zone. This is

maybe caused by the fact that we do not account for fluid and hydration processes in our models. The plate interface in our model is always severely overpressured ($\lambda = 0.95$) and heterogeneous which causes the slow slip events to form on the faultrock. Another reason could be the down-dip limit of the velocity weakening zone. To test whether the slow slip events do form below the seismogenic zone the down-dip limit of the velocity weakening can be removed and the fluid and hydration processes which are taken into account in the model of Van Dinther et al. [2013b] can be added to our model.

Multiple seismic and geodetic observations advocate that some slow slip events trigger earthquakes and that slipping patch of the earthquake partly overlaps with the area of slow slip [Romanet et al., 2018]. One example is the magnitude 7.3 Papanoa earthquake in the Cocos-North America subduction zone on 18 April, which was triggered by a slow slip event that began two months prior. The SSE was initiated in a region next to the earthquake and extended into the seismogenic zone, which caused an increase in stress in the hypocentral region or a weakening of this region [Radiguet et al., 2016].

In the STM-RSF model earthquakes are always preceded by slow slip events, which could be an indication that the SSE's indeed trigger earthquakes. The only problem is that the SSEs completely overlap with the earthquake nucleation zone and that they slip a large part of the seismogenic zone. On the slipping part of the megathrust the stress is decreased during the SSE, which has to increase again to the same level for the earthquake to occur. The nodes outside of the slipping area of the SSE are increased in stress, which could lead to a larger slipping area during the next event and could trigger an earthquake.

## 5.5   Limitations and future work

Even though many problems with the code were solved during my master thesis research there are still some issues that cause the models to quit or give output that is not compatible with nature or other studies. Most of them were already shortly discussed in the result section or other parts of the discussion, but here they will be analyzed in more detail.

First of all the velocities in the interseismic period are too high compared to the push velocity of 7.5 cm/yr that is imposed 500 kilometer before the trench. The slabs horizontal velocity increases landward and is 18 cm/yr just below the seismogenic zone (Fig. 10b), while it should decrease landward and be lower than the push velocity. The higher velocities are caused by fast movement of the mantle landward of the slab, this generates a pull on the slab towards the land and increases the velocities in the slab (Fig. 10b). The vertical velocity for the whole subducting plate and the continental plate until 1150 kilometers is upwards, after which it switches to downward (Fig. 10b). Both the upward and downward movement are caused by material flow in the lower boundary, which is vertically penetrable. The upward movement of the mantle seaward of the slab is already present in the long-term part (Fig. 10a), while the upward movement underneath the slab and the downward movement landward forms at the switch to rate- and state-dependent friction. It could be that the movement is caused by the slab cut off at 170 kilometers, which also occurs during the transition. Running a simulations without the cut off shows that the upward movement under the slab disappears, but the downward movement from 1150 kilometer is still present (Fig. 34). The velocity in the slab is closer to the push velocity, which is partly caused by the lower $W/h^*$ ratio of the simulation. This simulations eventually quits, while a simulation with the same friction parameters and no cut off is completed. So the slab cut off is not the main issue, but rather the downward movement from 1150 kilometers.

The interseismic period for the simulation used to analyse the slow slip events has a smaller horizontal velocity in the slab at the seismogenic zone and moves downward, which decreases to roughly no vertical movement deeper in the slab (Fig. 22) . The mantle landward of the slab moves towards the land as well, but the effect on the slab is less perceptible. The mantle underneath the subducting slab moves upwards, but the movement is minor at the 1300°C isotherm and is not passed on to the subducting plate. The mantle underneath the continental plate still moves downward. The only difference between the two models is the value of the direct-, evolutionary effect and the characteristic slip distance. The most important time step in the interseismic period is the healing time step (Eq. 32), which is calculated with the evolving state parameter. The state parameter is dependent on the characteristic slip distance and on the slip velocity (Eq. 26). How the changes in friction l parameters exactly influence the interseismic period is not clear yet, but could be proven by doing a more elaborated parameter study.
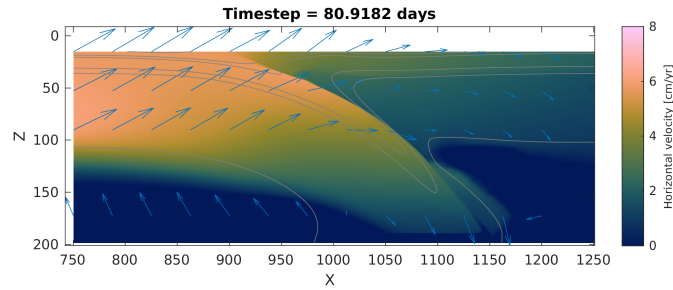
**Figure 34:** Velocity arrows plotted over the horizontal velocity for the interseismic period of the simulations without the slab cut-off.

Secondly, the model stops for simulations with too high slip rates due to waves originating from the lower boundary on the right (Fig. 13). The waves from the lower right boundary interfere with the propagation of the fault and eventually lead to failure of the simulation. There is one simulation that is not mentioned in this thesis, which has been able to reach the postseismic phase even though waves formed on the lower left boundary. This simulation has the same friction parameters of the simulation with the reference earthquake, but has a stronger lower crust and the maximum slip rate is around 10 m/s. The maximum slip rate of this simulation is lower than the slip rate of the models that fail, which is probably the reason that it can continue. The exact reason of the waves originating at almost the lower right boundary is not clear for me, but it is probably caused by the downward movement in the mantle and flow through the penetrable lower boundary.

Thirdly, there is no simulation that contains more than one earthquake, while in the seismic cycle model of Van Dinther et al. [2013a] 36 events are recorded in one simulation over 35,000 simulation years. The simulation with the reference earthquake has run for 5158 years without forming a second earthquake. Our modelling time is less than the STM model, but this is relative to the smaller time steps and is still large enough for a second earthquake to form for the Chillean subduction zone which has a recurrence interval of 300 year [Cisternas et al., 2005]. For both the STM model of Van Dinther et al. [2013a] and the strike-slip model of Herrendörfer et al. [2018] the first earthquake is more complex than the following are, because the system is highly stressed and not in balance before the first earthquake. We were only able to check the first earthquake, so it could be that its characteristics are exaggerated. The model does contain slow slip events before the earthquake which lowers the stress on the seismogenic zone. This makes it possible that the first earthquake is a good reference for the later earthquakes.

To overcome the above mentioned problems we can try to increase the modelling domain to 400 kilometers and change the lower boundary to free slip, which is now external free slip on 500 kilometer. By increasing the modelling depth the slab does not interact with the lower boundaries. Another solution would to decreases the long-term phase such that the slab does not interact with the lower boundary, which will be included in my guided research.

To test whether slow slip events will form below the downdip limit of the seismogenic zone the lower limit of velocity weakening has to be removed. For my master thesis I have not removed it, because I was afraid that the problems with the lower boundary would occur sooner.

Another addition to the model could be adding incoming sediments, such that the model setup is equal to the setup of Van Zelst et al. [2019] and more reflections form on the updip limit of the seismic zone.

The model was initially motivated to find out the origin of the secondary zone of uplift. The persistent existence of this zone was discovered by van Dinther et al. [2019], but only with the STM model they were not able to distinguish coseismic deformation from early postseismic deformation. Using our model it would be possible to distinguish the deformation in the different phases of the seismic cycle. I quantified the deformation and surface displacement for the different phases in my guided research report.

# 6    Conclusion

I succeeded to combine a geodynamic model of a subduction zone with a short-term seismic cycle. The invariant formulation of rate-and state-dependent friction together with the adaptive time stepping scheme Herrendörfer et al. [2018] decreases the time step during the coseismic period to milliseconds, which makes the slip rate equal to seismic values. The time step increases to an order of months during the interseismic period. The model solves the continuity and momentum equation for a visco-elasto-plastic rheology on a staggered grid with Lagrangian markers. The long term model takes up to 4 million years in which the oceanic slab slowly subducts into the mantle. When switching to the short-term seismic cycle the fault locks and loads stress at the plate interface.

In our reference simulations 250 years into the seismic cycle after the formation of two slow slip events an earthquake forms. The main earthquake is preceded by a fore-shocks at a depth of 60 kilometers. The megathrust starts to slip and the main earthquake nucleates 24 minutes after the fore-shock at a depth of 30 kilometers. From here the rupture propagates downward and upward into the sedimentary wedge until the sediment-basalt boundary. The rupture can't propagate into the sediments due to the higher cohesion and velocity strengthening behaviour. At a depth of 50 kilometers a back propagation occurs due to a lithological transition from basalt to sediments. These sediments were brought down in the long term phase from the sedimentary wedge, causing the seismogenic zone to be heterogeneous. The downdip limit of the megathrust increases with time during the earthquake and propagates into the transition area from velocity weakening to strengthening. The highest slip rate during the earthquake is 6.3 m/s, which is reached at a depth of 58 kilometers. The total time of the main earthquake is 100 seconds. The stress on the fault decreases mostly in the area between 30 kilometers in depth and the basalt-sediment boundary and in the area close to the lower limit of the seismic zone. The maximum drop in the second invariant of the deviatoric stress is 10 MPa, which is 5 MPa lower than the STM model. The changes in stress on the megathrust are heterogeneous, due to the presence of velocity strengthening sediment on the velocity weakening seismogenic zone. The largest increase in stress occurs downdip of the downdip limit of the seismic zone. Compared to seismic cycle model of Van Dinther et al. [2013b], the slip rates, time steps and duration of the events are much more realistic, which makes it possible to distinct early postseismic displacement from coseismic. In the coupled dynamic rupture of Van Zelst et al. [2019] the velocities are even higher, due to more reflections occurring in the sedimentary wedge.

With the STM-RSF model it is also possible to generate slow slip events, which can be classified in two classes. The first class has a maximum velocity in the order of $10^{-8}$ m/s, slips only the lower part of the fault, horizontal distance further than 940 kilometers, and takes years to complete. During the event both the subducting and continental plate move seaward due to push of the mantle underneath the continental plate. The second class has a maximum velocity in the order of $10^{-4}$ m/s, slips the whole megathrust and it takes multiple days to a month to complete. The pattern of the velocities is similar to a seismic event, but the velocity is 5 orders of magnitude smaller. The continental plate moves towards the sea and upward at the fault tip, while the subducting plate moves landward and partly down.

The slow slip events can form in a simulation that only contains slow slip events or before an fast earthquake. The behaviour of a simulation is defined by the characteristic slip distance and the seismic zone divided by the nucleation size ($W/h^*$), as in other studies. In our model four different regimes can be determined. The first regime is for $W/h^*$ values smaller than 6.2 and is characterised by stable sliding with a speed of $1.5 * 10^{-9}$ m/s. The second regime has a $W/h^*$ between 6.2 and 9.65 and contains periodic slow slip events, which can include one low magnitude seismic event. The third regime has a $W/h^*$ value between 9.65 and 15 and is characterised by multiple slow slip events with one earthquake, after which stable sliding starts. The last regime has a $W/h^*$ value above 15 and contains multiple earthquakes and slow slip events. These regimes are comparable to the regimes of Liu and Rice [2007], but the (a)periodic slow slip events have a larger maximum slip rate in our models and earthquakes nucleate for a lower $W/h^*$ ratio.

# References

Barbot, S., Lapusta, N., and Avouac, J.-P. (2012). Under the hood of the earthquake machine: Toward predictive modeling of the seismic cycle. *Science*, 336(6082):707–710.

Behr, W. M. and Bürgmann, R. (2021). What's down there? the structures, materials and environment of deep-seated slow slip and tremor. *Philosophical Transactions of the Royal Society A*, 379(2193):20200218.

Blaser, L., Krüger, F., Ohrnberger, M., and Scherbaum, F. (2010). Scaling relations of earthquake source parameter estimates with special focus on subduction environment. *Bulletin of the Seismological Society of America*, 100(6):2914–2926.

Cisternas, M., Atwater, B. F., Torrejón, F., Sawai, Y., Machuca, G., Lagos, M., Eipert, A., Youlton, C., Salgado, I., Kamataki, T., et al. (2005). Predecessors of the giant 1960 chile earthquake. *Nature*, 437(7057):404–407.

Dal Zilio, L., Lapusta, N., Avouac, J.-P., and Gerya, T. (2022). Subduction earthquake sequences in a non-linear visco-elasto-plastic megathrust. *Geophysical Journal International*, 229(2):1098–1121.

Den Hartog, S., Niemeijer, A., and Spiers, C. J. (2012). New constraints on megathrust slip stability under subduction zone p–t conditions. *Earth and Planetary Science Letters*, 353:240–252.

Dieterich, J. H. (1972). Time-dependent friction in rocks. *Journal of Geophysical Research*, 77(20):3690–3697.

Dieterich, J. H. et al. (1981). Constitutive properties of faults with simulated gouge. *Mechanical behavior of crustal rocks*, 24:103–120.

Fagereng, Å., Hillary, G. W., and Diener, J. F. (2014). Brittle-viscous deformation, slow slip, and tremor. *Geophysical Research Letters*, 41(12):4159–4167.

Gerya, T. (2019). *Introduction to numerical geodynamic modelling*. Cambridge University Press.

Gerya, T. (2022). Numerical modeling of subduction: State of the art and future directions. *Geosphere*, 18(2):503–561.

Gerya, T. V. and Yuen, D. A. (2003). Characteristics-based marker-in-cell method with conservative finite-differences schemes for modeling geological flows with strongly variable transport properties. *Physics of the Earth and Planetary Interiors*, 140(4):293–318.

Gerya, T. V. and Yuen, D. A. (2007). Robust characteristics method for modelling multiphase visco-elasto-plastic thermo-mechanical problems. *Physics of the Earth and Planetary Interiors*, 163(1-4):83–105.

Herrendörfer, R. (2018). *Modeling of the slip spectrum along mature and spontaneously forming faults in a visco-elasto-plastic continuum*. PhD thesis, ETH Zurich.

Herrendörfer, R., Gerya, T., and van Dinther, Y. (2018). An invariant rate-and state-dependent friction formulation for viscoeastoplastic earthquake cycle simulations. *Journal of Geophysical Research: Solid Earth*, 123(6):5018–5051.

Heuret, A., Lallemand, S., Funiciello, F., Piromallo, C., and Faccenna, C. (2011). Physical characteristics of subduction interface type seismogenic zones revisited. *Geochemistry, Geophysics, Geosystems*, 12(1).

Jarrard, R. D. (1986). Relations among subduction parameters. *Reviews of Geophysics*, 24(2):217–284.

Kajitani, Y., Chang, S. E., and Tatano, H. (2013). Economic impacts of the 2011 tohoku-oki earthquake and tsunami. *Earthquake Spectra*, 29(1_suppl):457–478.

Lapusta, N. and Liu, Y. (2009). Three-dimensional boundary integral modeling of spontaneous earthquake sequences and aseismic slip. *Journal of Geophysical Research: Solid Earth*, 114(B9).

Lapusta, N., Rice, J. R., Ben-Zion, Y., and Zheng, G. (2000). Elastodynamic analysis for slow tectonic loading with spontaneous rupture episodes on faults with rate-and state-dependent friction. *Journal of Geophysical Research: Solid Earth*, 105(B10):23765–23789.

Lavier, L. L., Tong, X., and Biemiller, J. (2021). The mechanics of creep, slow slip events, and earthquakes in mixed brittle-ductile fault zones. *Journal of Geophysical Research: Solid Earth*, 126(2):e2020JB020325.

Lay, T., Kanamori, H., Ammon, C. J., Nettles, M., Ward, S. N., Aster, R. C., Beck, S. L., Bilek, S. L., Brudzinski, M. R., Butler, R., et al. (2005). The great sumatra-andaman earthquake of 26 december 2004. *Science*, 308(5725):1127–1133.

Liu, Y. and Rice, J. R. (2007). Spontaneous and triggered aseismic deformation transients in a subduction fault model. *Journal of Geophysical Research: Solid Earth*, 112(B9).

Nakatani, M. (2001). Conceptual and physical clarification of rate and state friction: Frictional sliding as a thermally activated rheology. *Journal of Geophysical Research: Solid Earth*, 106(B7):13347–13380.

Radiguet, M., Perfettini, H., Cotte, N., Gualandi, A., Valette, B., Kostoglodov, V., Lhomme, T., Walpersdorf, A., Cabral Cano, E., and Campillo, M. (2016). Triggering of the 2014 mw7. 3 papanoa earthquake by a slow slip event in guerrero, mexico. *Nature Geoscience*, 9(11):829–833.

Rice, J. R., Lapusta, N., and Ranjith, K. (2001). Rate and state dependent friction and the stability of sliding between elastically deformable solids. *Journal of the Mechanics and Physics of Solids*, 49(9):1865–1898.

Romanet, P., Bhat, H. S., Jolivet, R., and Madariaga, R. (2018). Fast and slow slip events emerge due to fault geometrical complexity. *Geophysical Research Letters*, 45(10):4809–4819.

Rubin, A. M. and Ampuero, J. P. (2005). Earthquake nucleation on (aging) rate and state faults. *Journal of Geophysical Research: Solid Earth*, 110(B11).

Ruff, L. and Kanamori, H. (1980). Seismicity and the subduction process. *Physics of the Earth and Planetary interiors*, 23(3):240–252.

Saffer, D. M. and Wallace, L. M. (2015). The frictional, hydrologic, metamorphic and thermal habitat of shallow slow earthquakes. *Nature Geoscience*, 8(8):594–600.

Sato, M., Ishikawa, T., Ujihara, N., Yoshida, S., Fujita, M., Mochizuki, M., and Asada, A. (2011). Displacement above the hypocenter of the 2011 tohoku-oki earthquake. *Science*, 332(6036):1395–1395.

Seno, T. (2009). Determination of the pore fluid pressure ratio at seismogenic megathrusts in subduction zones: Implications for strength of asperities and andean-type mountain building. *Journal of Geophysical Research: Solid Earth*, 114(B5).

Sobolev, S. V. and Muldashev, I. A. (2017). Modeling seismic cycles of great megathrust earthquakes across the scales with focus at postseismic phase. *Geochemistry, Geophysics, Geosystems*, 18(12):4387–4408.

Uyeda, S. and Kanamori, H. (1979). Back-arc opening and the mode of subduction. *Journal of Geophysical Research: Solid Earth*, 84(B3):1049–1061.

Van Dinther, Y., Gerya, T., Dalguer, L., Mai, P. M., Morra, G., and Giardini, D. (2013a). The seismic cycle at subduction thrusts: Insights from seismo-thermo-mechanical models. *Journal of Geophysical Research: Solid Earth*, 118(12):6183–6202.

Van Dinther, Y., Gerya, T., Dalguer, L. A., Corbi, F., Funiciello, F., and Mai, P. M. (2013b). The seismic cycle at subduction thrusts: 2. dynamic implications of geodynamic simulations validated with laboratory models. *Journal of Geophysical Research: Solid Earth*, 118(4):1502–1525.

van Dinther, Y., Mai, P. M., Dalguer, L., and Gerya, T. (2014). Modeling the seismic cycle in subduction zones: The role and spatiotemporal occurrence of off-megathrust earthquakes. *Geophysical Research Letters*, 41(4):1194–1201.

van Dinther, Y., Preiswerk, L. E., and Gerya, T. V. (2019). A secondary zone of uplift due to megathrust earthquakes. *Pure and Applied Geophysics*, 176(9):4043–4068.

Van Zelst, I., Wollherr, S., Gabriel, A.-A., Madden, E. H., and van Dinther, Y. (2019). Modeling megathrust earthquakes across scales: One-way coupling from geodynamics and seismic cycles to dynamic rupture. *Journal of Geophysical Research: Solid Earth*, 124(11):11414–11446.

Vermeer, P. A. and De Borst, R. (1984). Non-associated plasticity for soils, concrete and rock. *HERON, 29 (3), 1984*.

Vigny, C., Socquet, A., Peyrat, S., Ruegg, J.-C., Métois, M., Madariaga, R., Morvan, S., Lancieri, M., Lacassin, R., Campos, J., et al. (2011). The 2010 m w 8.8 maule megathrust earthquake of central chile, monitored by gps. *Science*, 332(6036):1417–1421.

Wirth, E. A., Sahakian, V. J., Wallace, L. M., and Melnick, D. (2022). The occurrence and hazards of great subduction zone earthquakes. *Nature Reviews Earth & Environment*, 3(2):125–140.